ACERP
Advanced Ceramics Progress

Advanced Ceramics Progress

15:6:15:5:7.5 (Vol.%)

15:6:0:10:5 (Vol.%)

15:4:0:15:0 (Vol.%)

10:6:10:20:0 (Vol.%)

HfB_2-$MoSi_2$-ZrC-SiC-C_f after Oxidation at 1400 $^\circ$C for 2h

Materials and Energy Research Center

Iranian Ceramic Society

CONTENTS

Advanced Ceramics Progress

Research Article

Investigating the Kinetic Parameters of SiO_2-Al_2O_3-CaO-CaF_2-K_2O Oxyfluoride Glass

M. Soleymani Zarabad [a], M. Rezvani [a] *

[a] Department of Materials Science and Engineering, University of Tabriz, Tabriz, East Azerbaijan, Iran

A R T I C L E   I N F O

A B S T R A C T

Oxyfluoride glass-ceramics containing CaF_2 nanocrystals are kind of attractive materials for the optical applications due to their low phonon energy and high transparency. Moreover, the crystallization control and consequently, the kinetic properties are important for oxyfluoride glasses. Therefore, in the present research, the crystallization kinetics of isochronal transformation of the $37.26SiO_2$-$28.11Al_2O_3$-$7.73CaO$-$26.89CaF_2$-4.5 K_2O (wt%) glass have been determined upon the basis of maximum transformation rate using Differential Thermal Analysis (DTA) technique. Hence, it is concluded that the crystallization of the mentioned glass is a process controlled by Avrami nucleation, three-dimensional diffusion-controlled growth, and anisotropic growth impingement mode. The effective activation energy Q_P=181 kJ.mol^{-1}, growth exponent n=2.272, nucleation activation energy Q_N= 123, and growth activation energy Q_G=211 have been determined.

1. INTRODUCTION

Rare-earth doped glass-ceramics have been developed for different optical devices such as optical fiber, optical amplifier, infrared, visible laser, and specially night vision cameras [1, 2]. Fluoride glasses and their crystals indicate a high transparency in infrared to the ultraviolet region [3, 4] in addition to the low phonon energy (<500cm^{-1}) [5, 6]. However, they have low chemical and mechanical stability and thus, their preparation is highly limited [7]. Oxyfluoride glass-ceramics were developed to overcome the drawbacks of silicate glasses and fluorides as the hosts of rare-earth ions [8, 9]. Nucleation and growth of fluoride crystals, such as CaF_2, occur in the parent glass matrix during the heat treatment and rare-earth ions preferentially segregate into these fluoride crystals [1]. The crystallization process in amorphous materials provides the interesting aspects of solid states phase transformation. The transformation kinetics model of Johnson-Mehl-Avrami-Kolmogorov (JMAK) describes the transformation of a material into another phase during an isochronal or isothermal phase

transformation as a function of temperature and time, respectively, which can be used when the JMA model cannot be used [10]. This model was modified to Liu-Sommer-Mittemeijer (LSM). The evaluation of the maximum transformation rate was used for isochronal and isothermal transformations including different modes of nucleation, growth, and impingement. This method has been applied to determine the impingement mode and consequently, the activation energies for nucleation and growth separately. This method has been used successfully on the Mg–Cu–Y metallic glass crystallization [11].

In this research, the Aluminosilicate based oxyfluoride glasses with $37.26SiO_2$-$28.11Al_2O_3$-$7.73CaO$-$26.89CaF_2$ (wt%) composition were prepared through the conventional melt-quenching method. This composition was selected since the aluminosilicate based glass can provide necessary optical transparency and strength for optical applications. In addition, the glass can maintain transparency after the heat treatment for crystallization of fluoride nanocrystals [7, 8]. The non- isothermal kinetics analysis known as LSM (Liu-Sommer-Mittemeijer)

∗ Corresponding Author Email: m_rezvani@tabrizu.ac.ir (M. Rezvani)

based on maximum transformation rate [12, 13] was applied for the oxyfluoride glasses to investigate the crystallization kinetic and to determine the impingement mode, growth exponent, and separate activation energies of nucleation and growth.

2. EXPERIMENTAL PROCEDURE

$37.26SiO_2$-$28.11Al_2O_3$-$7.73CaO$-$26.89CaF_2$-$4.5K_2O$ (wt %) glasses were prepared using precursor powders. The mentioned composition is the most typical one for the basic glass, which has also been used by other scientists [14- 18]. The main starting materials are high purity leached SiO_2 (99% purity), Al_2O_3 (Merck 101077), and CaF_2 (Dae Jung 2508145). $CaCO_3$ (Merck 102069) and K_2CO_3 (Sigma-Aldrich P5833) were applied to introduce CaO and K_2O. To avoid bubbles in the samples, Sb_2O_3 and As_2O_3 were used as refining agents. K_2O was added to the batch to have a melt with favorable viscosity [18]. 50g of the batch was mixed and poured in alumina crucibles, heated with the rate of $10°C.min^{-1}$, and finally melted at 1723K (1450°C) for 1 hour in an electric furnace.

Then melt was poured into the preheated stainless steel molds, which were heated at 773K (500°C) and used to shape the molten glass, then were cooled in air. Finally, obtained glassy discs with a thickness as much as 0.5cm were annealed at 773K (500°C) for 30 min to release the internal stresses arose from thermal shock.

The crystal phase analysis of glass-ceramics was carried out by X-Ray diffraction (XRD, Siemens D-500). In this research, the X-ray diffraction just used to ensure that there is not any crystallization during the cooling procedure of the melt and to determine the crystal structure of the crystallized phase after heat treatment.

The differential thermal analysis (DTG- 60AH Shimadzu) of powdered glass samples was carried out through different heating rates of 5, 10, 15 and $20°C.min^{-1}$ to determine the crystallization temperatures. About 50mg of powdered glass was analyzed by differential thermal analysis (DTA) for Kinetic calculations to investigate the crystallization behavior.

The sample preparation for scanning electron microscopy (SEM) included polishing, etching in a 5% HF solution for 30 seconds and finally applying gold-coat. Subsequently, the SEM observations of the prepared sample were carried out through Tescan MIRA3 FEG- SEM.

3. RESULTS AND DISCUSSION

The composition of glass $37.26SiO_2$-$28.11Al_2O_3$-$7.73CaO$-$26.89CaF_2$-$4.5K_2O$ (wt %) is shown in Table 1.

TABLE 1. Composition of the glass $37.26SiO_2$-$28.11Al_2O_3$-$7.73CaO$-$26.89CaF_2$-$4.5K_2O$

		Composition (wt %)				
SiO_2	Al_2O_3	CaO	CaF_2	K_2O	As_2O_5	Sb_2O_5
37.26	28.11	7.73	26.89	4.5	0.2	0.2

The melted oxyfluoride glass was heat-treated at about Tp (based on DTA results) to determine the crystalline phase. Figure 1 (a) and (b) show the image of oxyfluoride glass and XRD patterns of the as-prepared and the heat-treated glasses at 952K for 1h, respectively. The amorphous structure of as-prepared sample and the crystalline peaks of the heat-treated sample (indexed as CaF_2 crystals) are illustrated in Figure 1 (b).
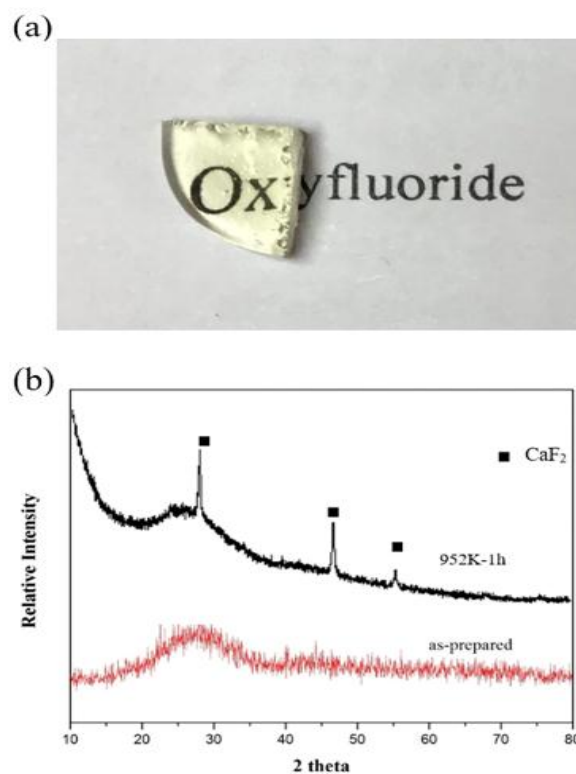
Figure 1. (a) Photograph of as-prepared oxyfluoride glass and (b) XRD patterns of oxyfluoride glass and glass-ceramic which are heat-treated at 952K (T_{p1}) for 1h

About 20mg powder samples were poured in a standard platinum crucible and scanned in room temperature to complete crystallization at different heating rates from 5 to 20 $K.min^{-1}$. DTA curves were studied for determination of the crystallization temperature and studying of kinetic properties. Figure 2 shows a series of DTA curves measured at different heating rates (Φ) of 5,

10, 15, and 20 K.min^{-1}. Table 2 illustrates the summarized information of Figure 2 including the glass transition temperature (T_g), the onset temperature of the first phase crystallization (T_{ost}), the maximum crystallization temperature of the first phase (T_{p1}), and the crystallization temperature of the second phase (T_{p2}). The first peak is attributed to the crystallization of CaF_2 at the heating rate of 10K min^{-1} and temperature about 952K and the second one is related to the crystallization of $Ca_2Al_3O_6F$ at a temperature about 1179K [19].
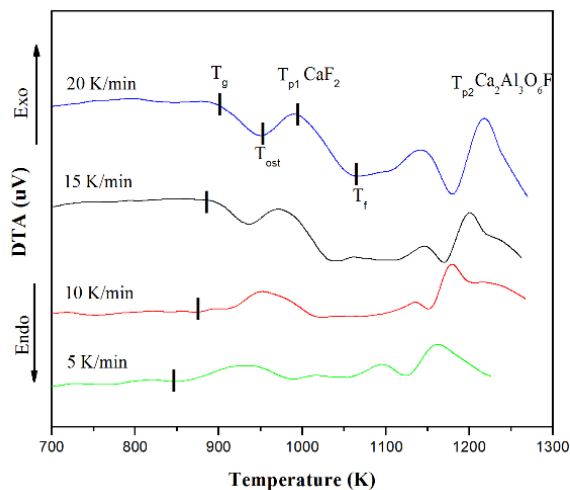
Figure 2. DTA curves of the oxyfluoride glass measured at different heating rates

According to the DTA results, all of the above characteristic temperatures increase by increasing the heating rate (Φ), which illustrate that the crystallization of these two phases is a kinetic process. , The kinetic properties of CaF_2 phase will be studied due to its optical importance. The crystallization fraction f is f= (AT/A) at a given temperature of T. Where A is the total area of the exothermic peak between Tost (where the crystallization begins) and Tf (where the crystallization completes) and AT is the area between Tost and desired temperature T.

TABLE 2. Characteristic temperatures values of the glass at different heating rates

Φ (K min^{-1})	T_g /K	T_{ost}/K	T_{p1}/K	T_{p2}/K
5	843	870	932	1161
10	874	911	952	1179
15	884	932	971	1200
20	899	962	990	1218

The transformed fraction, which does not overlap the new phase particles is given in the form of equation (1) [12].

$$X_e = (k\alpha)^n = \left(K_0 \alpha exp \left(-\frac{Q}{RT} \right) \right)^n \qquad (1)$$

Where α represents RT^2/Φ for isochronal transformation's and K_0 is the rate constant and the pre-exponent factor of the rate constant, respectively. Q stands for the effective activation energy and n shows the growth or Avrami exponent. T, t, R, and Φ are the temperature, time, gas constant, and constant heating rate, respectively. In this model, the impingement mode would result in the real transformed fraction (f). The transformation degree (f) is related to the extended transformation degree (X_e) by impingement modes (random nuclei dispersion, anisotropic growth, non-random nuclei).

The evolution of df/dT versus T (Figure 3(a)) was carried out using f versus T (Figure 3(b)) and the df/dT versus f (Figure 3(c)) for the crystallization of 37.26SiO$_2$-28.11Al$_2$O$_3$-7.73CaO-26.89CaF$_2$-4.5K$_2$O (wt %) oxyfluoride glass system. The f_p (a quantity for f at maximum transformation rate) values were obtained from the graphs and listed in Table 3.

TABLE 3. The values of f_p, and n_p

Φ/K min^{-1} (°C min^{-1})	T_p	f_p	ξ	n_p
5	932	0.6131	1.1086	2.105
10	952	0.6040	1.1632	2.236
15	971	0.5778	1.3342	2.332
20	990	0.5585	1.4772	2.416

It has been found out that f_p values are less than 0.632 for all different transformations rates, which means that prevailing impingement mode is due to the anisotropic growth According to the impingement mode equations, which are mentioned above, the position of transformation rate maximum (f_p) will increase in the case of "non-random nuclei dispersion" with increasing ε and the position of transformation rate maximum (f_p) will decrease in case the of "anisotropic growth impingement" with increasing ξ [11]. So from the position of f_p, the values of ξ and ε (impingement factors) can be determined.

(a)

(b)

(c)
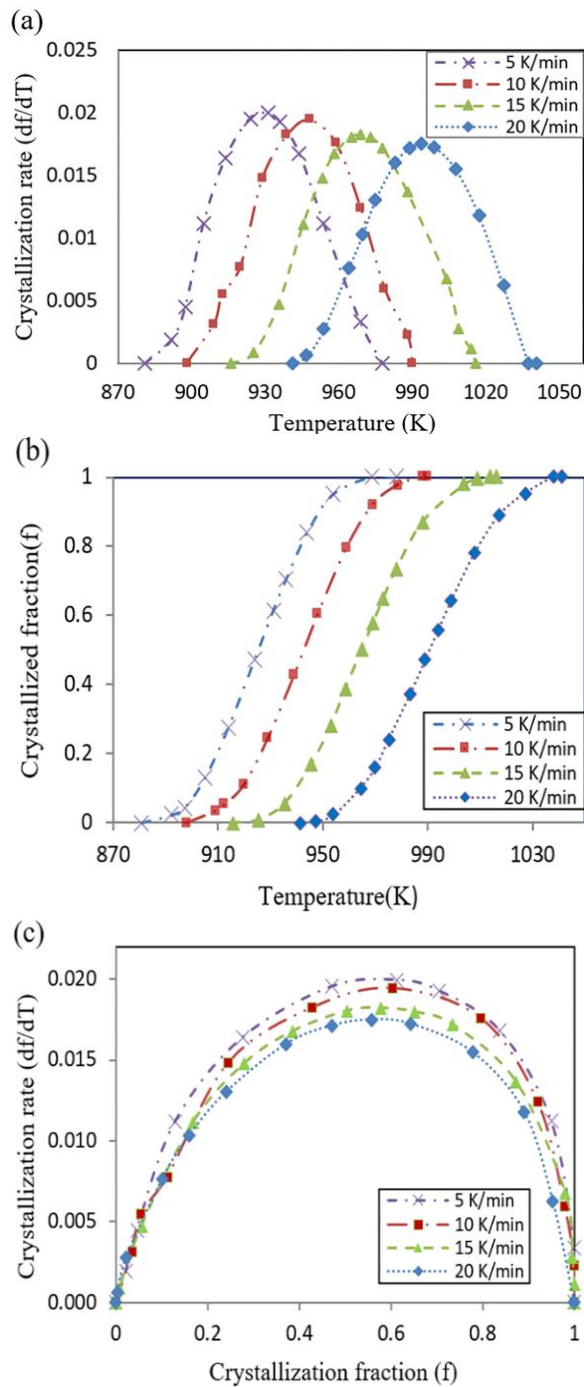
Figure 3. Evolution of: (a) df/dT versus T, (b) f versus T and (c)df/dT versus f for isochronal transformation of $37.26SiO_2$-$28.11Al_2O_3$-$7.73CaO$-$26.89CaF_2$-$4.5K_2O$ glass system (Φ=5, 10, 15 and 20 (℃/min))

As shown in Figure 4, anisotropic growth impingement is prevailing at $37.26SiO_2$-$28.11Al_2O_3$-$7.73CaO$-$26.89CaF_2$-$4.5K_2O$ glass system with the decreasing values of fp with increasing the ξ. Moreover, Figure 5 shows the cross-sectional SEM image of the glass

system, which is heat-treated for 1h at Tp. The values of ξ for different heating rates are listed in Table 3.
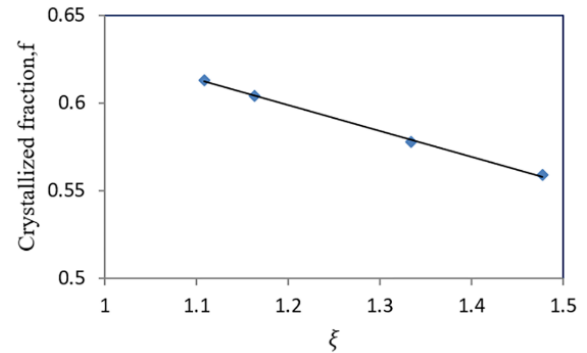
Figure 4. Evolution of f versus ξ for $37.26SiO_2$-$28.11Al_2O_3$-$7.73CaO$-$26.89CaF_2$-$4.5K_2O$ glass system

Further kinetic information can be obtained using maximum transformation rate analyzing after determination of the impingement mode. With regard to isochronal analysis, the np value is obtained from the equation (2).

$$n_p = \frac{RT_p^2}{Q_p + 2RT_p}\left(\frac{d\,lnX_e}{dT}\right)_p \tag{2}$$
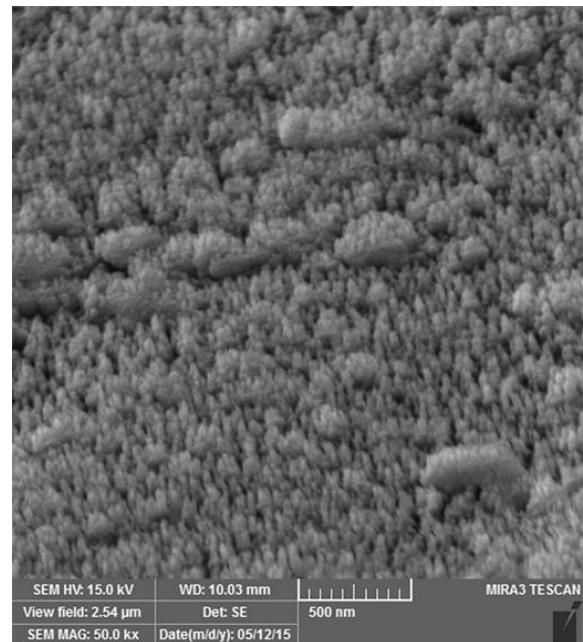
Figure 5. Cross-sectional SEM image of $37.26SiO_2$-$28.11Al_2O_3$-$7.73CaO$-$26.89CaF_2$-$4.5K_2O$ glass-ceramic

Although the expression of Xe follows from the identified different impingement mode in Equations (2)-(5) in isochronal transformations, the quantity of Q_p is necessary to determine the np value. The value of Q_p can be determined using a Kissinger-like analysis as equation (3) [12, 13].

$$\frac{d\left(ln\frac{RT_p{}^2}{\Phi}\right)}{d\left(\frac{1}{T_p}\right)} = \frac{Q_p}{R} \qquad (3)$$

As it is shown in Figure 6, Q_p is calculated around 181 kJ.mol^{-1} from the slope of the $ln\frac{RT_p{}^2}{\Phi}$ versus $\frac{1}{T_p}$ plot by applying Equation 10 to the data in Figure 6. After np, the growth exponent was obtained using Equation 9 and the data were listed in table 3. The isochronal annealing results in Refs. [11, 12, 20] show an increase in np along with increasing the Φ, which is compatible with Avrami nucleation. The data in Table 3 show that np increases with increasing the Φ in this oxyfluoride glass system. Crystallization mechanism of CaF_2 in oxyfluoride glasses is a three-dimensional, volume diffusion-controlled growth process [20].

Figure 6. Determination of effective activation energy from the data in Figure 3

According to volume diffusion-controlled growth theory, the Avrami exponent is described as equation (4) [21].

$$n = a + bm \qquad (4)$$

Where a is nucleation index (a=0 when nucleation is zero, a>1 for the increasing nucleation rate, 0<a<1 when the nucleation rate is decreasing, and a=1 for the constant nucleation rate), b is the dimensionality of growth (b=1,

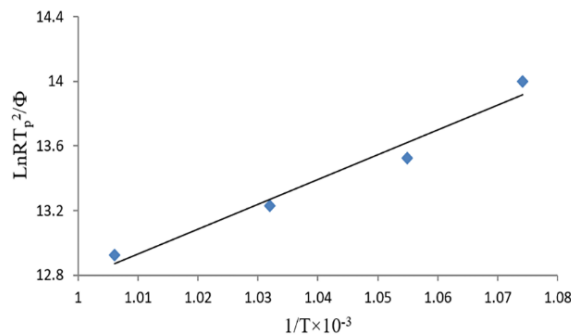2, or 3 for one-dimensional, two-dimensional, or three-dimensional growth respectively), and m is growth index (m=0.5 is for diffusion-controlled growth mode and m=1 is for interface controlled growth mode). In the Avrami exponent, n for this oxyfluoride system varies from 2.10 to 2.42. The average Avrami exponent about 2.272 gives b=3, m=0.5, and 0<a<1, which implies the main diffusion-controlled three-dimensional growth with an Avrami decreasing nucleation rate during the crystallization. As shown in Table 3, the value of n for the oxyfluoride amorphous glass increases with increasing the heating rate. According to the DTA curves in Figure 2, it is clear that the transformation temperature increases with increasing the heating rate. Therefore, the values of n increase with increasing transformation temperature because the atomic diffusion is difficult at low temperatures, which results in retardation of nucleation and growth process and leads to a lower nucleation rate. At higher transformation temperatures, the diffusion of atoms will be relatively easy, which will increase the nucleation rate. It means that the nucleation and growth rates are not constant during the crystallization process.

The value of effective activation energy Q_p, which is obtained using Equation 10 and the maximum transformation rate data from Figure 3 is about 181 kJ.mol^{-1}.

As mentioned before, an equation can be used to determine the activation energy of nucleation Q_N with consideration the Avrami nucleation for this oxyfluoride system [10] as equation (5).

$$ln\left(\frac{\alpha}{\frac{1}{n_p - {}^d/_m} - 1}\right) = -\ln A + Q_N/R\,T_P \qquad (5)$$

plotting $ln\left(\frac{\alpha}{\frac{1}{n_p - {}^d/_m} - 1}\right)$ vs $1/Tp$. Where α is identified as RT^2/Φ for isochronal transformations and m is the growth mode parameter, which is equal to 2 for volume diffusion-controlled growth and d is the dimensionality of growth, which is equal to 3 in this system. It is concluded that d/m=3/2, so Q_N=123 kJ.mol^{-1} is obtained.

Then Q_G follows from equation (6) [12].

$$Q_G = \frac{n_p(Q_p - Q_n)}{{}^d/_m} + Q_N \qquad (6)$$

According to the obtained results for Q_p and np and using equation 6, the Q_G value is obtained as much as 211 kJ.mol^{-1}.

The characteristic parameters of the process are determined through fitting the numerical description of

the transformation basis with experimental data in principle, which are physically significant [10]. From the above obtained kinetic information of $37.26SiO_2$-$28.11Al_2O_3$-$7.73CaO$-$26.89CaF_2$-$4.5K_2O$ glass system, it is argued that the crystallization of mentioned system is governed by Avrami nucleation, three-dimensional diffusion-controlled growth, and anisotropic growth impingement mode. Accordingly, a new equation will be obtained considering Equation 1 and fraction transformed during impingement due to anisotropic growth.

$$f = 1 - \left\{ 1 + (\xi - 1)\left[k_0^n \left(\frac{RT^2}{\Phi} \right)^n exp\left(-\frac{nQ}{RT} \right) \right] \right\}^{\frac{-1}{\xi - 1}} \quad (7)$$

Consequently, the exact kinetic data was obtained by fitting the resulting equation (equation 7) with experimental data of f versus T and df/dT versus T (Figure 3a and Figure 3b). The obtained kinetic data of K_0^n, n, Q are shown in Table 4. The resulted values of n and Q are compatible with obtained experimental data from analysis of maximum transformation rate. This also proves that the isochronal crystallization mechanism of $37.26SiO_2$-$28.11Al_2O_3$-$7.73CaO$-$26.89CaF_2$-$4.5K_2O$ glass is based on Avrami nucleation, three-dimensional diffusion-controlled growth, and anisotropic growth impingement mode

TABLE 4. Model parameters determined by fitting the curve of *f* versus *T* and df/dT versus T for the $37.26SiO_2$-$28.11Al_2O_3$-$7.73CaO$-$26.89CaF_2$-$4.5K_2O$ glass system, which was crystallized by the mechanism of Avrami nucleation, three-dimensional diffusion-controlled growth, and anisotropic growth impingement mode

Parameter	K_0^n	n	Q (kJ.mol^{-1})	Error%
Value	3.77E+10	2.457	183.44	0.65

4. CONCLUSION

According to the analytical phase transformation model, the kinetic data of the isochronal crystallization of $37.26SiO_2$-$28.11Al_2O_3$-$7.73CaO$-$26.89CaF_2$-$4.5K_2O$ (wt %) glass have been determined. The crystallization of the mentioned glass is a process controlled by Avrami nucleation, three-dimensional diffusion-controlled growth, and anisotropic growth impingement mode. The effective activation energy, growth exponent, nucleation activation energy, and growth activation energy have been determined as much as Q_P=181 kJ.mole^{-1}, n=2.272, Q_N= 123, Q_G=211, respectively.

REFERENCES

1. Lavín, V., Lahoz, F., Martín, I. R., Rodríguez-Mendoza, U. R., "Optical properties of rare-earth ions in transparent oxyfluoride glass-ceramics", In Balda, R., ed., **Photonic Glasses, Research Signpost,** Kerala, India, (2006), 115-149. https://www.academia.edu/download/46573097/54-Photonic_Glasses_Chapter_6.pdf

2. Upadhyaya, G. S., "**Holland, W., Beall, G.: Glass-Ceramic Technology, "The American Ceramic Society", Westerville, OH, USA, 2002, pp. 372**", **Science of Sintering**, Vol. 36, No. 3, (2004), 215-216. https://doi.org/10.2298/sos0403216u

3. Gonçalves, C. M., Santos, L. F., Almeida, R. M., "Rare-earth-doped transparent glassceramics", **Comptes Rendus Chimie**, Vol.5, No. 12, (2002), 845–854. https://doi.org/10.1016/S1631-0748(02)01457-1

4. Farahinia, L., Rezvani, M., "Luminescence Properties of Oxyfluoride Glass and Glass-ceramic Doped with Y^{3+} Ions", **Advanced Ceramics Progress**, vol. 1, No. 1, (2015), 6-10. https://dx.doi.org/10.30501/acp.2015.70000

5. Adam, J, L., "Non-oxide glasses and their application in optics", **Journal of Non-Crystalline Solids**, Vol. 287, No. 1-3, (2001), 401–404. https://doi.org/10.1016/S0022-3093(01)00632-9

6. Adam, J. L., "Lanthanides in Non-Oxide Glasses", **Chemical Reviews**, Vol. 102, No. 6, (2002), 2461–2476. https://doi.org/10.1021/cr010305b

7. Dejneka, M. J, "Transparent oxyfluoride glass ceramics", **Materials Research Society Bulltin**, Vol. 23, No. 11, (1998), 57–62. https://doi.org/10.1557/s0883769400031018

8. Qiao, X., Fan, X., Wang, M., "Luminescence behavior of Er^{3+} in glass ceramics containing BaF_2 nanocrystals", **Scripta Materialia**", Vol. 55, No. 3, (2006), 211-214. https://doi.org/10.1016/j.scriptamat.2006.04.023

9. Ye, S., Zhu, B., Chen, J., Luo, J., Qiu, J. R., "Infrared quantum cutting in Tb^{3+}, Yb^{3+} co-doped transparent glass ceramics containing CaF_2 nanocrystals", **Appllied Physics Letters**, Vol. 92, No. 14, (2008), 141112. https://doi.org/10.1063/1.2907496

10. Moharram, A. H., Abdel-Baset, A. M., Shokr, F. S., "Crystallization kinetics of the $Se_{80}Te_{15}Sb_5$ glass", **Chalcogenide Letters**, Vol. 13, No. 9, (2016), 435–442. http://chalcogen.ro/435_MoharramAH.pdf

11. Liu, F., Song, S. J., Sommer, F., Mittemeijer, E. J., "Evaluation of the maximum transformation rate for analyzing solid-state phase transformation kinetics", **Acta Materialia**, Vol. 57, No. 20, (2009), 6176–6190. https://doi.org/10.1016/j.actamat.2009.08.046

12. Liu, F., Sommer, F., Bos, C., Mittemeijer, E. J., "Analysis of Solid State Phase Transformation Kinetics: Model and Recipes", **International Materials Reviews**, Vol. 52, No. 4, (2007), 193-212. https://doi.org/10.1179/174328007X160308

13. Mittemeijer. E. J., "Analysis of the kinetics of phase transformations", **Journal of Materials Science**, Vol. 27, No. 15, (1992) 3977-3987. https://doi.org/10.1007/bf01105093

14. Kishi, Y., Tanabe, S., "Infrared-to-visible up-conversion of rare-earth doped glass ceramics containing CaF_2 crystals", **Journal of Alloys and Compounds**, Vol. 408, (2006), 842-844. https://doi.org/10.1016/j.jallcom.2005.01.096

15. Babu, P., Jang, K. H., Kim, E. S, Shi, L., Seo, H. J., "Optical Properties and White-Light Emission in Dy^{3+}-Doped Transparent

Oxy-fluoride Glass and Glass Ceramics Containing CaF_2 Nanocrystals", *Journal of the Korean Physical Society*, Vol. 54, No. 4, (2009), 1488-1491. https://doi.org/10.3938/jkps.54.1488

16. Sun, X. Y., Gu, M., Huang. S. M, Jin, X. J., Liu, X. L., Liu, B., Ni, C., "Luminescence behavior of Tb^{3+} ions in transparent glass and glass-ceramics containing CaF_2 nanocrystals", *Journal of Luminescence*, Vol. 129, No. 8, (2009), 773-777. https://doi.org/10.1016/j.jlumin.2009.02.017

17. Sun, X. Y. and Huang. S. M., "Tb^{3+}-activated SiO_2–Al_2O_3–CaO–CaF_2 oxyfluoride scintillating glass ceramics", *Nuclear Instruments and Methods in Physics Research Section A: Accelerators, Spectrometers, Detectors and Associated Equipment*, Vol. 621, No 1-3, (2010), 322-325. https://doi.org/10.1016/j.nima.2010.04.032

18. Farahinia, L., Rezvani, M., "Optical property evaluation of oxy-fluoride glasses doped with different amounts of Y^{3+} ions",

Journal of Non-crystalline Solids, Vol. 425, (2015), 158-182. https://doi.org/10.1016/j.jnoncrysol.2015.03.014

19. Imanieh, M. H., EftekhariYekta, B., Marghussian, V., Shakhesi, S., Martín, I. R., "Crystallization of nano calcium fluoride in CaF_2–Al_2O_3–SiO_2", *Solid State Sciences*, Vol. 17, (2013) 76–82. https://doi.org/10.1016/j.solidstatesciences.2012.11.008

20. Liu, F., Sommer. F., Mittemeijer, E. J., "Analysis of the kinetics of phase transformations; roles of nucleation index and temperature dependent site saturation and recipes for the extraction of kinetic parameters", *Journal of Materials Science*, Vol. 42, No. 2, (2007), 573-587. https://doi.org/10.1007/s10853-006-0802-4

21. Ouyang, Y., Wang, L., Chen, H., Cheng, X., Zhong, X., Feng, Y., "The formation and crystallization of amorphous $Al_{65}Fe_{20}Zr_{15}$", *Journal of Non-Crystalline Solids*, Vol. 354, No.52-54, (2008), 5555-5558. https://doi.org/10.1016/j.jnoncrysol.2007.02.099

Advanced Ceramics Progress

Research Article

Electrodeposited Hydroxyapatite/Graphene Oxide/Zirconia Oxide Composite Coatings: Characterization and Antibacterial Activity

A. Khalili [a], F. Naeimi [b] *, A. A. Fakhrizadeh [b]

[a] *Department of Biomedical Engineering, South Tehran Branch, Islamic Azad University, Tehran, Tehran, Iran*
[b] *Advanced Materials Research Center, Materials Engineering Department, Najafabad Branch, Islamic Azad University, Najafabad, Isfahan, Iran*

ARTICLE INFO

ABSTRACT

The current study aimed to characterize the hydroxyapatite, zirconia, and graphene oxide nanocomposite coatings on titanium substrate by the use of electrophoretic deposition. In the first stage, besides the characterization of the created composite coating, the thickness and uniformity of the created coating were evaluated by the use of Scanning Electron Microscope (SEM). Also, the distribution of the Nano-powder particles was investigated by the elemental analysis. In the second stage, by the use of X-ray diffraction analysis, the position of the materials used in the coating was drawn and investigated. In the third stage, in order to evaluate the coating's corrosion behavior due to the addition of nanoparticles to the hydroxyapatite and compare it with the non-coated sample, the electrochemical analyses in the form of chemical polarization were investigated and analyzed with drawing the related charts. Finally, in the fourth stage, the antibacterial tests on the Escherichia coli and Staphylococcus bacteria on the coating were conducted and compared to the uncoated alloy samples. The corrosion test results indicated that the use of nano-composite coating leads to the increase in corrosion resistance of the surface. The antibacterial tests results demonstarted that the use of nano-composite coating effectively decreases the bacteria growth on the surface.

1. INTRODUCTION

Today, pure and alloy titanium are widely used for orthopedic materials and dental applications. The high corrosion resistance (due to formation of titanium oxide layer on the surface), proper mechanical properties (elastic modulus similar to the bone, the high strength to weight ratio), suitable biocompatibility with the tissue, great bone conduction, and the low toxicity are among the reasons behind the extensive use of this type of alloy. The hydroxyapatite coating is used to increase the titanium bonding with the tissue. Chemically and biologically, this material is highly similar to the bone and hard tissues of human. In spite of the proper performance of the hydroxyapatite coatings on the alloy surface from the biological point of view, another challenging subject is the structural fragility of this coating and investigation of its behavior in presence of infectious bacteria. The research show that the use of secondary materials such as titanium oxide, gelatin, chitosan, carbon nanotubes and graphene oxide can properly promote the mechanical behavior of this coating.

According to the research, the use of graphene oxide leads to the creation of a denser coating and sites for the germination of the hydroxyapatite crystals. On the other hand, the increase in the hardness and the elastic modulus are among the advantages of the production of this composite. The use of graphene oxide leads to the increase in coating's corrosion resistance. In the current study, the graphene oxide, zirconium oxide, and hydroxyapatite were combined by Electrophoretic method. Although the basic phenomenon which occurs in the Electrophoretic is well known, and it has been the main subject of many practical and theoretical studies, the ceramics electrophoretic was first studied by Hamaker [1]. The electrophoretic deposition is one of the colloid processes in production of the ceramics and has advantages such as the short formation time, simple facilities, low constraints compared to the substrate

shape, and no need for binder (which makes the amount of organic matter in the raw material very low or even zero) [2, 3].

The electric field effective on the electrophoretic is reduced by the deposition time, since an insulating layer is made of ceramic particles on the electrodes. However, during the first electrophoretic stage, a linear relationship between the deposition mass and the time is established [4]. Negishsi et al. observed that N-propanol's solvent flow density is comparable with the applied voltage in presence of any powders, and it becomes unstable with the increase in applied voltages. Such stable data are considered as a good guideline for the decision-making on the deposition parameters and the resultant quality of the sediment created by electrophoretic method [5].

The results obtained from different research show that this type of reinforcements causes problems and disorders. For example, addition of the carbon nanotubes causes biological disorders and adverse effects. After the conducted investigations, an absorbent material named graphene was noted. Graphene oxide has unique properties such as proper mechanical properties, great biocompatibility, good antimicrobial property, etc. Addition of graphene oxide to hydroxyapatite leads to the strengthening of the mechanical properties as well as the reduction in the surface cracks and the increase in adhesive strength of the coating. Ming et al. [6] deposed the graphene as the reinforcement to the hydroxyapatite on the titanium substrate by the electrophoretic deposition method. Li and Shei [7] in two articles, studied the antibacterial behavior of four types of graphene (graphite/graphite oxide/ graphene/ graphene derivative) to resist E.coli. It was revealed in this study that graphene oxide solvent has the highest antibacterial activity. Saberi et al. [8] prepared alcoholic suspensions of the zirconium nanoparticles and added Triethanolamine as a stabilizer to it. It was concluded that Triethanolamine is an effective stabilizer for ethanol suspensions with 0.45 density, Isopropanol suspension with 0.3 density, and Butanol suspension with 0.15 density. The current study aimed to characterize the hydroxyapatite, zirconia, and graphene oxide nanocomposite coatings on titanium substrate by the use of the impedance method.

2. MATERIALS AND METHODS/EXPERIMENTAL PROCEDURE

The chemical composition of the alloy used in the current study is provided in Table 1. The samples are abraded by the Sic-contained abrasive papers Nos. 400, 600, 800, and 1200, respectively. The samples were immersed in distilled water for 30 minutes in an ultrasonic apparatus to be degreased, and finally, they were rinsed by acetone.

TABLE 1. The Ti-6AL-4V alloy properties used in the current study

Element	Percentage
Vanadium	4.5
Aluminum	6.75
Iron	3
Oxygen	2
Carbon	0.8
Nitrogen	0.5
Hydrogen	0.15

The properties of the hydroxyapatite powder, zirconium oxide powder, and graphene oxide powder are presented in Table 2.

TABLE 2. The properties of the primary materials' powders used in the current study

Material name	Company	Molecular weight (g/mol)	Chemical formula
Hydroxyapatite	Sigma-Aldrich (US)	502.31	$Ca_{10}(po_4)_6OH_2$
Zirconia oxide	Merck (Germany)	123.21	Zro_2
Graphene oxide	Sigma-Aldrich (US)	120.52	GO

For the preparation of the suspension, the chosen composition powder including the hydroxyapatite is mixed with graphene oxide and zirconium oxide and 50ml of isopropanol obtained from Merck of Germany, and it was put on the magnetic stirrer. In order to better dissolve and create a positive charge on the surface of the hydroxyapatite particles, in addition to increasing the suspension stability, moving the particle toward the cathode and precipitating on its surface in the electrophoretic process of the specified amount, Merck's triethanolamine was added. Then it was put on the stirrer for 48 hours, and by the use of nitric acid, which was again obtained from Merck, the suspension's PH was set as around 3-4.

TABLE 3. The materials used in the suspension for electrophoretic process

Row	Composition name	Amounts
1	Isopropanol	50ml
2	Hydroxyapatite	0.3g
3	Graphene oxide	0.01g
4	Zirconium oxide	0.02g
5	TEA	2ml

In order to create the composite coating, firstly, the intended electrodes were prepared and then, by connecting to the power supply and placing it in a suspension solution with a specified voltage of 60 V and a predetermined time of 180 seconds, the coating was applied to the surface. The voltage selection and coating time were determined based on the optimal conditions. Then, in order to create stability and increase the resistance and adhesion of the applied composite coating, the sintering operation was used. To do so, the coated sample was put in the vacuum oven with a temperature of 950 centigrade for 2 hours, and then it was cooled in the oven.

Elemental analysis was performed by the EDAX EDS Silicon Drift 2017 detector. In order to investigate the crystal structure of the synthesized powders, the X-ray diffraction machine Philips, model Xpert with 31mA current and 41kW voltage was used. The cathode lamp used was copper with a wavelength of 1,4114 angstroms. Scan rate of 1 and step size of 1.11 / s were selected. The phase detection was done by the X-pert software.

For performing the electrochemical tests, first, the metal samples were degreased by the alcohol and then they were rinsed by distilled water. Each of the samples was used as the working electrode after preparation on the cell, and were added to the counter for completion of the circuit and conducting the test. Then, the intended solution was injected into the cell and for setting the temperature, a heating system which included a thermal element and thermometer was used. Potentiostat-galvanostat IVIUMSTAT with IVIUMSOFT software was used for electrochemical measurements by the use of electrochemical polarization spectroscopy method. For performing the antibacterial test, it is required to do the preparations 24 hours prior to the test. To do so, the needed cultivation environments are prepared and for sterilizing these environments, they were put into the autoclave for 15 minutes at a temperature of 121 centigrade. Also, the case and control samples are both sterilized. To prepare the bacteria needed, they are passaged 24 hours before the test.

In order to perform the test by the passaged colonies, we prepare the intended suspension. For suspension preparation with the 10^8 cfu/ml concentration, it is required to be compared to the McFarland standards (to prepare this solution, we add 0.05ml of the $BaCl_2$ 1% solution to 0.95ml of H_2so_4 1% solution and stir well). In order to determine the precise number of the bacteria by the spectrophotometry machine, we measure its absorption rate. The absorption rate required for 10^8 cfu/ml concentration is 625 nanometers. We add 1 cc of the suspension with the intended dilution to the alloy's surface (the pure titanium alloy has been considered as the control sample). Then, it is pit inside an incubator with a temperature of 37 centigrade for 24 hours. In the following, we collect the bacteria from the alloy's surface by a sampler, and add them to a tube which contains 100 cc of ringer cultivation environment, and the vortex it. Then, we prepare the 10^5, 10^6, and 10^7 concentrations through dilution and culture them by the use of spread-plate method. After closing the plates, we put them inside an incubator with a temperature of 37 centigrade, and after 24 hours, we count the colonies by the colony counter and report the number. The bacteria used in this test were gram-positive (E-coli) with ATTC29213 and gram-negative (S-Areus) with ATTC25922.

3. RESULTS AND DISCUSSION

The current study aimed to characterize the hydroxyapatite, zirconia and graphene oxide nanocomposite coatings on titanium substrate by the use of the impedance method. Firstly, besides the characterization of the created composite coating, the thickness and uniformity of this coating were measured by the use of SEM. Then, by the use of X-ray diffraction test, the position of the used materials in the coating was investigated and in the next stage, the electrochemical tests in the form of chemical impedance were performed to evaluate the corrosion behavior of the coating and compare it with the uncoated sample. In the final phase, by performing the antibacterial tests on the E.Coli and S.Areus on the created coating, it was evaluated and compared to the uncoated alloy sample.

3.1. Evaluation of the Coating Structure and Morphology

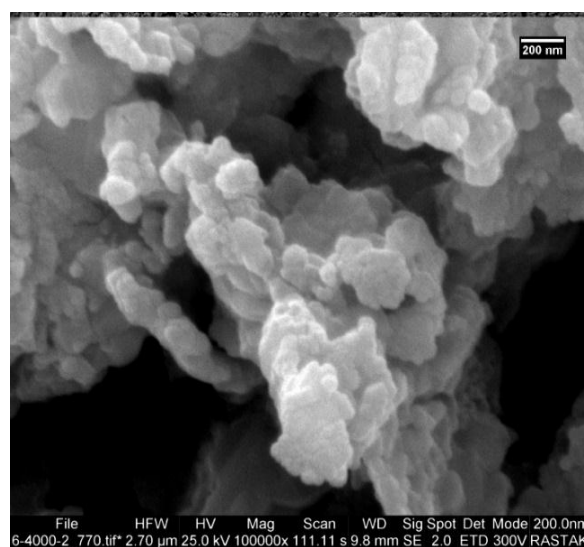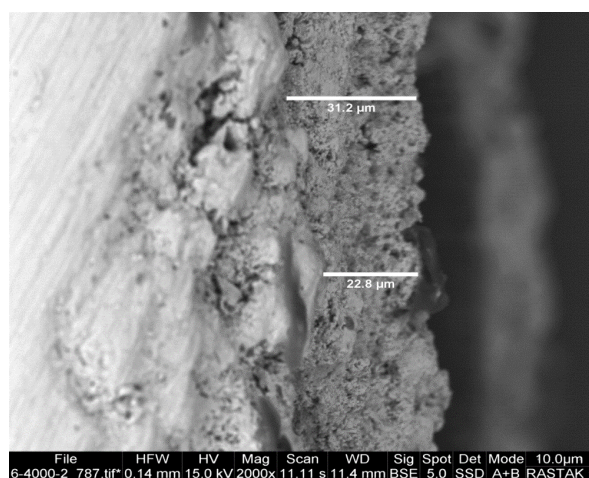The images taken from the coating by the SEM are provided in Figures of 1 and 2.

Figure 1. SEM micrograph of the coated sample

The studies show that the hydroxyapatite coating shows weak mechanical and antibacterial properties, and one of the proper ways to promote this costing's properties is the production of the coating with a secondary phase, which shows better properties compared to the pure hydroxyapatite coating. The uniform morphology and the agglomeration of the used powder can be seen in the image. The results indicate that the use of a secondary phase creates the adhesion to the substrate and higher uniformity as well as a surface with no cracks. The investigations show that the factors effective on the thickness of the created composite coatings by the electrophoretic method, depend on the parameters such as the time, voltage, and type of the composition. In Poorraeisi et al study titled "characterization and coating of the hydroxyapatite-zirconium oxide-titanium oxide nanocomposite" observed that by addition of zirconium to pure hydroxyapatite and increasing the voltage, the coating's thickness is increased [9].

As was observed, time and voltage are two effective factors in the electrophoretic method. With the passage of time and increase in the voltage, an optimal coating would be obtained and the more these two parameters are increased, the thicker the sample would be [10].

substrate. The peaks intensity was proportionate to the weight percentage of each element in the composite formation. In the composite compound, the amount of the nanohydroxyapatite powder which includes calcium, phosphorus, hydrogen, and oxygen, is higher. The next point is that in these samples, due to having coatings in common with gold peaks, the palladium peak was used to avoid the homogeneity of the peaks.

According to Figure 4, the elemental analysis along the coating has been presented based on different elements. The presence of coating's constituent elements confirms the type of coating's composition.

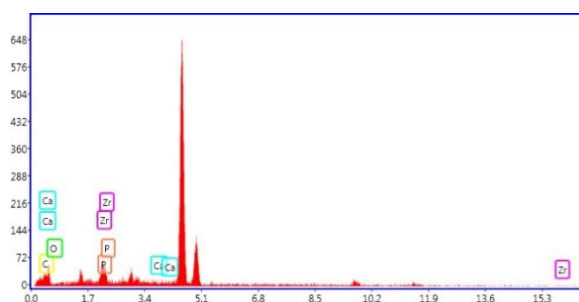**Figure 3.** EDAX analysis of the composite coating

Figure 2. SEM micrograph of the cross-section of composite coating

According to the results, the coating has a thickness of 22.8 to 31.2 micrometers. The results also showed that coating distribution on different sections of the surface has a specific range.
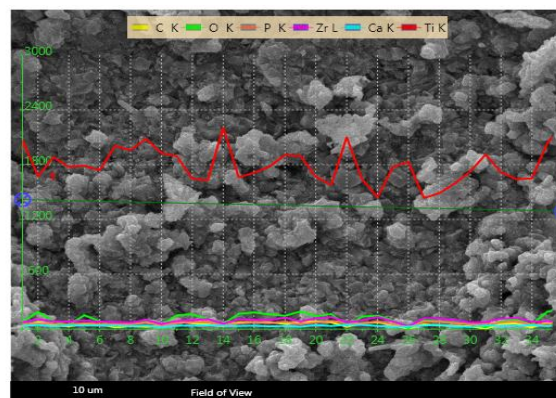
Distribution of the elements in coating was analyzed by the EDAX analyzer for the hydroxyapatite/zirconium oxide composite coating and the graphene oxide on the titanium substrate (Figure 3). Based on the obtained results, we can observe that all elements of the composite have been successfully distributed on the titanium

Figure 4. The distribution of the hydroxyapatite, zirconium, and graphene oxide composite coating's elements

According to Figure 5, the distribution of the various elements in the MAP test on the coating's surface has been presented. Also, as observed, the distribution of the secondary phases elements on the surface has been suitable. In the current study, the graphene oxide has been added to the composite as a reinforcement, which can be seen in black.
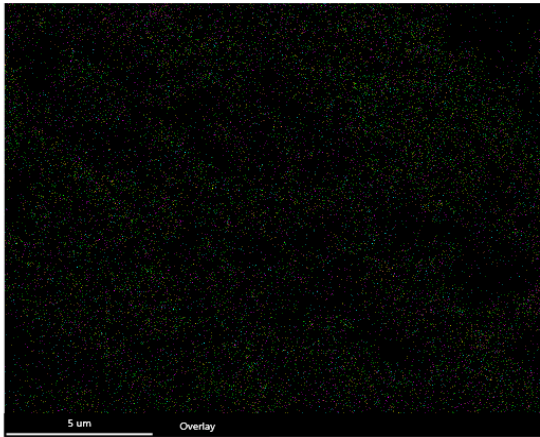
Figure 5. MAP image of various elements of the composite surface

3.2. Phase Evaluation

The X-ray diffraction machine has been used for phase detection of the coatings. Ming et al. in an article titled "characterization of the hydroxyapatite-graphene oxide composite coating by the electrophoretic method" found out that by addition of the graphene oxide to the hydroxyapatite powder, the peaks intensity is increased and the more the graphene oxide is added, the higher the intensity will be.

As observed in Figure 6, all the peaks of the composite coating have been precisely drawn and each of the compositions has been drawn based on the peak's intensity and hardness. It should be noted that regarding the fact that the hydroxyapatite powder in this composite coating has been used more than the other materials, the coating is significant on all the points.

The comparison of the obtained peaks with the JCPDS standard cards shows that all the available phases on the coating are in the XRD spectrum. The existing elements are calcium, phosphorus, oxygen, carbon, zirconium oxide, and titanium.
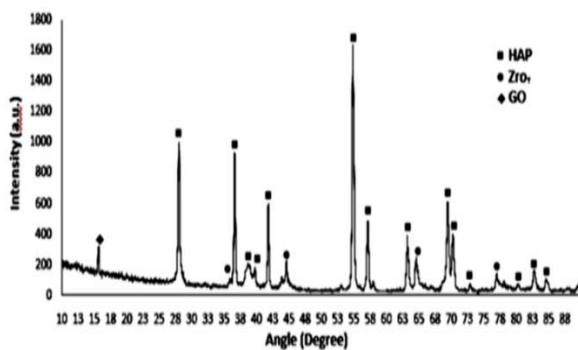

Figure 6. The X-ray diffraction pattern for the hydroxyapatite/graphene oxide/zirconium oxide composite

3.3. Evaluation of Coating Corrosion Resistance

Hadidi et al. in an article titled "synthesis of the hydroxyapatite/copper and hydroxyapatite/copper oxide nanocomposites by the electrophoretic method" concluded that hydroxyapatite -5% copper has the lower corrosion current density and as a result, the highest resistance to the corrosion in the hydroxyapatite/copper oxide coatings [11]. In addition, by increasing the copper oxide percentage in the coating, due to more nobility of the copper oxide, the coatings corrosion potential is more positive.

Evaluation of the two samples showed that in the Figure 7, by the impedance electrochemical tests, it can be concluded that corrosion resistance in the samples with the composite coating is significantly increased compared to the uncoated samples, and it can lead to the increase in the properties and higher efficiency of this type of coating.
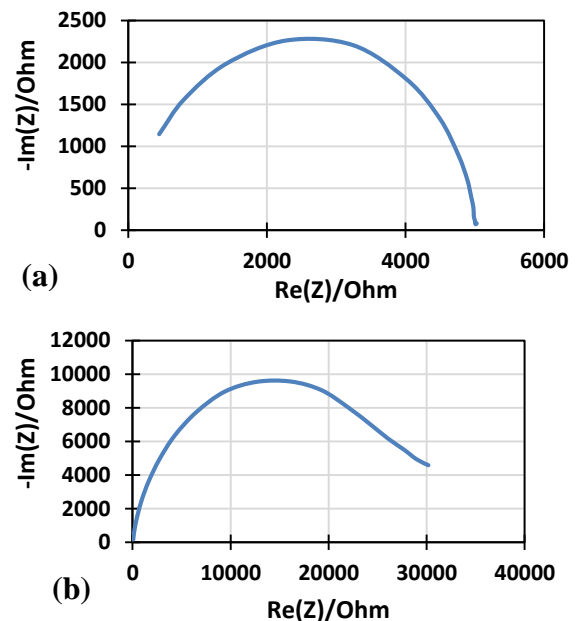
Figure 7. The impedance electrochemical test performed in the study (a) Ti-6Al-4V substrate without coating and (b) the coated sample

3.4. Antibacterial Behavior Evaluation

In the microbial discussion, the bacteria are generally formed on the composite coatings in the form of a biofilm. The formation of the bacteria can damage the coated surface and lead to penetration of the bacteria inside it, which would consequently lead to defections on the surgery point or breakage of the implant. Therefore, it is needed to combine new composite materials which have both bioactive and antibacterial properties. Numerous methods and research have been conducted by the scientists in the microbial fields and the ways to

confront them (antibacterial). During the conducted studies, numerous composites such as the hydroxyapatite/graphene, hydroxyapatite/graphene/chitosan, etc. could not increase the antimicrobial property. With the research done by the researcher, a ceramic material named zirconium was added to the hydroxyapatite/graphene oxide composite, and then the results and images of the study were recorded.

Jancovich et al. in a study titled "characterization of the hydroxyapatite/chitosan nanocomposite and graphene oxide coatings by the electrophoretic method" concluded about the antibacterial property that by addition of the graphene oxide powder to the hydroxyapatite/chitosan compound, the number of the bacteria has been significantly reduced compared pure hydroxyapatite [12]. Based on this research, the results show that by addition of the zirconium oxide to the coating's composite, the antibacterial properties can be improved.

Based on the results obtained, it was observed that the S.Areus bacteria count reached 2.45×10^6 cfy/ml which means that it has been significantly decreased.

As observed in Figures of 8 and 9, the hydroxyapatite coating is susceptible to microbial contamination. Also, in terms of mechanical properties, it is too weak. The graphene oxide is added to the hydroxyapatite as a reinforcement. Both mechanically and biologically, it has been increased. By addition of the zirconium oxide, the antibacterial properties of the nanocomposite coating have been significantly increased and improved.
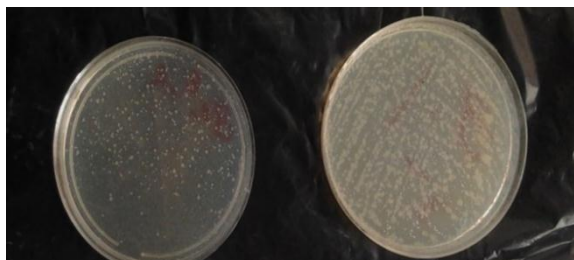
Figure 8. Results of the antibacterial activity tests of the composite coated sample (E. coli bacterial cells)
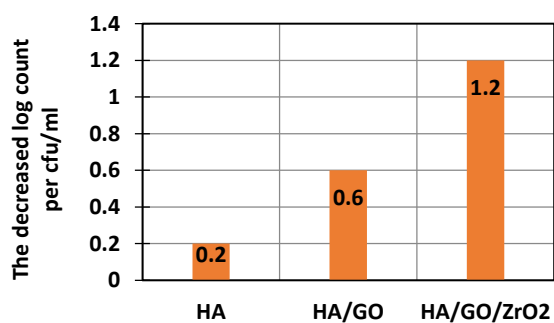
Figure 9. The effects of the use of zirconium oxide on the antimicrobial properties

4. CONCLUSION

The current study aimed to characterize the hydroxyapatite, zirconium oxide, and graphene oxide nanocomposite coating on the titanium substrate by the use of the electrophoretic deposition. The results indicated that this coating has a thickness of around 22.8-31.2 micrometers. Also, the substructure of the created coatings was uniform and free of microscopic cracks. All the elements of the composite coating were also visible. The impedance electrochemical test results also showed that the corrosion resistance of the samples with the mentioned composite coating has been significantly increased compared to the uncoated samples, and it can lead to the increase in the properties of this type of coating and higher efficiency of it. Also, all the peaks of the hydroxyapatite/zirconium oxide/graphene oxide composite elements are visible (carbon, calcium, zirconium, oxygen, phosphorus, hydrogen, and titanium). Finally, the results indicated that the effects of the creation of a hydroxyapatite/zirconium oxide/graphene oxide composite coating increase the antibacterial properties.

ACKNOWLEDGEMENT

REFERENCES

1. Hamaker, H. C., "Formation of a deposit by electrophoresis", *Transactions of the Faraday Society*, Vol. *35*, (1940), 279-287. https://doi.org/10.1039/TF9403500279

2. Diba, M., Fam, D. W. H., Boccaccini, A. R., Shaffer, M. S. P., "Electrophoretic deposition of graphene-related materials: A review of the fundamentals", *Progress in Materials Science*, Vol. 82, (2016), 83-117. https://doi.org/10.1016/j.pmatsci.2016.03.002

3. Sarkar, P., Nicholson, P. S., "Electrophoretic deposition (EPD): mechanisms, kinetics, and application to ceramics", *Journal of the American Ceramic Society*, Vol. 79, No. 8, (1996), 1987-2002. https://doi.org/10.1111/j.1151-2916.1996.tb08929.x

4. Zhitomirsky, I., Gal-Or, L., "Electrophoretic deposition of hydroxyapatite", *Journal of Materials Science: Materials in Medicine*, Vol. *8, No.* 4, (1997), 213-219. https://doi.org/10.1023/A:1018587623231

5. Vandeperre, L., Van der Biest, O., Clegg, W. J., "Silicon carbide laminates with carbon interlayers by electrophoretic deposition", In Fuentes, M., Martínez-Esnaola, J. M., Daniel, A.M., (eds.), *Key Engineering Materials*, Vol. 127-131, Trans Tech Publications Ltd., Switzerland, (1997), 567-574. https://doi.org/10.4028/www.scientific.net/kem.127-131.567

6. Li, M., Liu, Q., Jia, Z., Xu, X., Cheng, Y., Zheng, Y., Xi, T., Wei, S., "Graphene oxide/hydroxyapatite composite coatings fabricated by electrophoretic nanotechnology for biological applications", *Carbon*, Vol. 67, (2014), 185-197. https://doi.org/10.1016/j.carbon.2013.09.080

7. Hu, W., Peng, C., Luo, W., Lv, M., Li, X., Li, D., Huang, Q., Fan, C., "Graphene-based antibacterial paper", **ACS Nano**, Vol. 4, No. 7, 4317-4323. https://doi.org/10.1021/nn101097v

8. Saberi, F., Boroujeny, B. S., Doostmohamdi, A., Baboukani, A. R., Asadikiya, M., "Electrophoretic deposition kinetics and properties of ZrO_2 nano coatings", **Materials Chemistry and Physics**, Vol. 213, (2018), 444-454. https://doi.org/10.1016/j.matchemphys.2018.04.050

9. Poorraeisi, M., Afshar, A., "The study of electrodeposition of hydroxyapatite-ZrO_2-TiO_2 nanocomposite coatings on 316 stainless steel", **Surface and Coatings Technology**, Vol. 339, (2018), 199-207. https://doi.org/10.1016/j.surfcoat.2018.02.030

10. Shi, Y. Y., Li, M., Liu, Q., Jia, Z. J., Xu, X. C., Cheng, Y., Zheng, Y. F., "Electrophoretic deposition of graphene oxide reinforced chitosan–hydroxyapatite nanocomposite coatings on Ti substrate",

Journal of Materials Science: Materials in Medicine, Vol. 27, No. 3, (2016), 48. https://doi.org/10.1007/s10856-015-5634-9

11. Hadidi, M., Bigham, A., Saebnoori, E., Hassanzadeh-Tabrizi, S. A., Rahmati, S., Alizadeh, Z. M., Nasirian, V., Rafienia, M., "Electrophoretic-deposited hydroxyapatite-copper nanocomposite as an antibacterial coating for biomedical applications", **Surface and Coatings Technology**, Vol. 321, (2017), 171-179. https://doi.org/10.1016/j.surfcoat.2017.04.055

12. Janković, A., Eraković, S., Mitrić, M., Matić, I. Z., Juranić, Z. D., Tsui, G. C., Tang, C. Y., Mišković-Stanković, V., Rhee, K. Y., Park, S. J., "Bioactive hydroxyapatite/graphene composite coating and its corrosion stability in simulated body fluid", **Journal of Alloys and Compounds**, Vol. 624, (2015), 148-157. https://doi.org/10.1016/j.jallcom.2014.11.078

Advanced Ceramics Progress

Effect of Heat Treatment on Grain Growth of Magnetic Nanocrystalline Hydroxyapatite Powder

S. Kouhkanzadeh [a], I. Mobasherpour [a] *, M. J. Molaei [b], E. Salahi [a], M. Pazouki [c]

[a] Department of Ceramic, Materials and Energy Research Center, Meshkindasht, Alborz, Iran
[b] Faculty of Chemical and Materials Engineering, Shahrood University of Technology, Shahrood, Semnan, Iran
[c] Department of Energy, Materials and Energy Research Center, Meshkindasht, Alborz, Iran

A B S T R A C T

Nanocrystalline Magnetic Hydroxyapatite (MHAp) was synthesized through co-precipitation method and the subsequent heat treatment. Phase analysis, particle morphology, chemical bonding, and magnetic properties were studied using XRD, FESEM, FTIR, and VSM, respectively. The XRD results showed that MHAp was formed by heat treatment at 1100 °C. The samples heat-treated at 500 and 1100 °C incorporated a plate-like morphology with a mean crystallite size of 11.7 and 59.9 nm, respectively. In addition, the VSM results indicated that the synthesized MHAp was characterized by magnetic features after heat treatment. According to the findings in this study, the coercive field (H_c), saturation magnetization (M_s), and magnetism stayed (M_r) were 0.175 kO$_e$, 0.00147, and 0.02615 emug^{-1}, respectively, in -10 to 10 kO$_e$ magnetic field. The growth kinetics of the MHAp was alo studied. According to the results, the growth activation energies for low and high temperatures were 45.51 and 67.33 kJ/mol, respectively. Owing to several properties already proven, the MHAp powder was successfully synthesized.

https://doi.org/10.30501/acp.2020.241694.1040

1. INTRODUCTION

Apatite-group minerals are of great economic and scientific significance due to their low cost, availability, and ease of use [1]. HAp is a mineral that consists of phosphate and calcium which can be found in animal and human hard tissues such as mammalian teeth, vertebrate bones, mature teeth of some chiton species, and fish scales [2]. HAp with the space group of P63/m, has a hexagonal crystal structure. The unit cell of the HAp consists of six PO_4^{3-}, ten Ca^{2+}, and two OH^-. The ion exchange strength of metal ions with Ca^{2+} makes HAp capable of immobilizing the heavy metal ions in water sources [3]. Apatite can be produced by a co-precipitation synthesis method using phosphate and calcium. HAp with the chemical formula of $Ca_{10}(PO_4)_6(OH)_2$-A has been extensively used for

removing the contaminants from aqueous solutions [1]. The HAp is also efficient in the removal of different heavy metal ions such as lead, cadmium, copper, nickel, zinc, uranium, and cobalt from aqueous solutions. This material enjoys several advantages including low solubility in water, good buffering characteristics, and high stability during oxidation, making it a promising substance for the recovery of the heavy metal ions from aqueous solutions [4].

Utilization of magnetic nanoparticles in different applications such as wastewater treatment, biomedical, and catalyst support has been extensively investigated in recent years. Among the magnetic nanoparticles, magnetic HAp has attracted considerable attention due to its excellent metal ions adsorption, hyperthermia characteristics, biocompatibility, low cost, and eco-friendliness [5]. The synthesis of iron oxides and HAp

nanoparticles have been thoroughly investigated by several researchers worldwide. However, investigation of the synthesis of magnetic HAp is limited to fewer studies [6]. Different synthesis routes were employed to produce the magnetic HAp. It can be synthesized by the substitution of transition metal ions into the HAp crystal structure. It was observed that the substitution of Fe^{2+}, Co^{2+}, and Mn^{2+} ions into the crystal structure of the HAp would result in the magnetic moments of 4, 3, and 5 Bohr magnetons, respectively [7]. The magnetic HAp can also be synthesized by making composites of magnetic materials and HAp. Different magnetic nanoparticles such as Fe_3O_4 [8-11], $MgFe_2O_4$ [12], $CoFe_2O_4$ [13], $NiFe_2O_4$ [14], and $ZnFe_2O_4$ [15] were utilized to synthesize the magnetic HAp. Different synthesis methods were also employed to produce the magnetic HAp including microwave-assisted route [16], mechano-chemical [17], precipitation followed by hydrothermal [18], and co-precipitation [1].

The present study aims to synthesize the magnetic HAp through the co-precipitation method. The effect of heat treatment temperature on phase composition was also investigated. In addition, the grains growth kinetics was explored. Moreover, the growth constants and activation energy of the growth were obtained.

2. MATERIALS AND METHODS

2.1. Materials

Ferric chloride hexahydrate ($FeCl_3.6H_2O$, Merck Art no. 231-729-4), iron (II) chloride tetrahydrate ($FeCl_2.4H_2O$, Merck Art no. 231-843-4), diammonium hydrogen phosphate ((NH_4)$_2HPO_4$, Merck Art no. 231-987-8), calcium nitrate ($Ca(NO_3)_2$, Merck Art no. 233-332-1), and Ammonia solution 25% (NH_4OH, Merck Art no. 1054321000) were used in the present study without further purifications. All of the prepared solutions were used without storage time. All glassware was rinsed with distilled water and dried before use.

2.2. Preparation of magnetic HAp nanoparticles

Synthesis of the magnetic HAp nanoparticles was performed through the co-precipitation method. First, 0.4107, 1.1057, 8.96, and 23.81 gr of ferrous chloride, ferric chloride, diammonium hydrogen phosphate, and calcium nitrate were weighed, respectively. Ferrous chloride and ferric chloride were added to 30 ml distilled water and mixed in 30 minutes. At the same time, calcium nitrate and diammonium hydrogen phosphate were added to 250 ml distilled water and mixed in 30 minutes. After the preparation of the solutions, Iron chloride and calcium nitrate solutions were added and

mixed together. The mixture was stirred for 5 minutes. In the next step, diammonium hydrogen phosphate solution was added as the same time as NH_4OH was used to adjuste pH 11 at room temperature. By adding NH_4OH, the color of the initial solution turned from light brown to black. Each uncolored drop of diammonium hydrogen phosphate turned white by dropping into the black solution that finally changed the whole solution color. Th final solution rested for 24 hours. After rest, the light brown sediment was deposited at the end of the balloon which was covered by uncolored liquid. Sediment was separated by centrifuge at 4000 rpm for 10 minute and was dried in oven for 24h at 90°C. The process was followed by heat treatment at 500, 700, 900, and 1100°C, and, 1100°C for an hour in a tube furnace. Total heat treatment time was 3 hours with a heating rate of 10 K/min.

2.3. Instrumentation

Synthesized powders were analyzed by X-Ray Diffraction (XRD) (Siemens D-500, Cu-K_α radiation λ=1.54 A°, 30KV. in Bragg- Brentano geometry (θ-2θ)), one of the most exclusive equipment used for analysis and specific determination of crystals properties such as diagnosis of the phases, size and, distance among the crystalline layers in crystals. During the heat treatment, phase transformations and change in the size of crystals were expected and the extent of these changes was estimated using the XRD results and Scherrer method [19]:

$$t = \frac{0.9\lambda}{B\cos\theta} \tag{1}$$

where (t) is the average crystallite size (nm), λ is the Cu$K\alpha$ wave length (nm), B is the diffraction peak width in a half maximum intensity (radian), and θ is the Bragg diffraction angle.

Samples were sent for Fourier Transform Infrared Spectroscopy (FT-IR) test to characterize the composition and confirm the XRD results. The FT-IR test was performed by Bruker's infrared vector 33 spectroscopy device in the range of 4000-400 cm^{-1} of wavenumber. Synthesized MHAp was observed by SEM (MIRA3TEScan, HV: 15.0 KV). The magnetic properties were checked by Vibrating Sample Magnetometer (VSM) (Magnetic Daghigh Kavir type MDKB) that operates based on Faraday's imposing law.

3. RESULTS AND DISCUSSION

3.1. Characterization of MHAp

Fig. 1 compares the results obtained from X-ray test of heat treatment powders at different temperatures of 500, 700, 900, and 1100°C for 1 hour by Xpert software. As observed, the amorphous magnetite hydroxyapatite phase was formed at the lowest temperature of the heating process. Heat treatment at 700°C revealed the same result as 500°C. At a temperature of 900°C, Tri-Calcium Phosphate (TCP) phase was formed in the presence of the MHAp phase. The presence of the iron element in the environment system reduced the decomposition temperature of the hydroxyapatite to the TCP phase [20]. Increasing the temperature of the system led to an increase in the intensity peak of tricalcium phosphate. The peaks shown in the MHAp and TCP phases in 1100°C were sharper mainly due to theirs higher degrees of crystallization. On the contrary, at 1100°C, the graph moved slightly to the left due to the presence of iron at the site of the cations in the hydroxyapatite structure. Finally, the results of the sample heated at 1100°C temperature for an hour showed that a majority of the hydroxyapatite markers in other samples were converted to tricalcium phosphate, indicating a phase transformation and excessive decomposition of hydroxyapatite to tricalcium phosphate at this temperature.
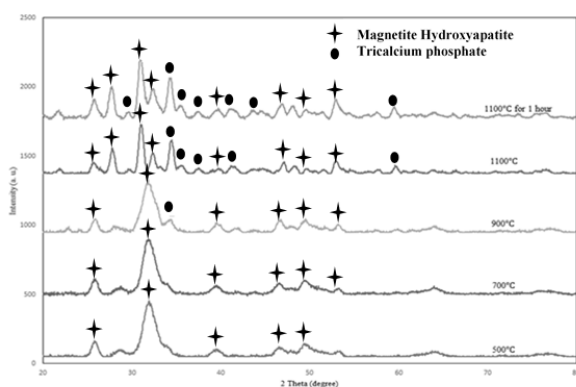
Figure 1. XRD results of the heat treatment magnetic hydroxyapatite powders at 500, 700, 900, 1100, and 1100°C for 1 hour

In Table 1, the crystallite size of MHAp as a function of heat treatment based on the XRD profile analysis were shown. To calculate the size of crystals, a method based on Scherrer's method and an expert software were employed. It was observed that as temperature increased

from 500°C up to 1100°C, the crystallite size of magnetic hydroxyapatite increased.

**TABLE 1.** The crystallite size of MHAp crystalline as a function of heat treatment

No.	Temperature [°C]	Crystallite size [nm]
1.	500	11.70
2.	700	18.70
3.	900	32.90
4.	1100	59.90

Examination of FT-IR powder test results is also an affirmation for XRD results. In the infrared spectroscopic spectrum, a series of absorption bands were observed in the middle region of infrared waves. As illustrated in Fig. 2, the adsorption band 1043 cm^{-1} represents the P-O bond [21]. Although sharp peaks such as 548 and 607 cm^{-1} indicate O-P-O bond in hydroxyapatite [22], peak 548 cm^{-1} represents Fe-O bond in Hydroxyapatite structure [23]. The peak ranges of 887, 919, and 1043 cm^{-1} show the P-O bond, and the peak of 3423 cm^{-1} represents O-H bond in this composition [21].
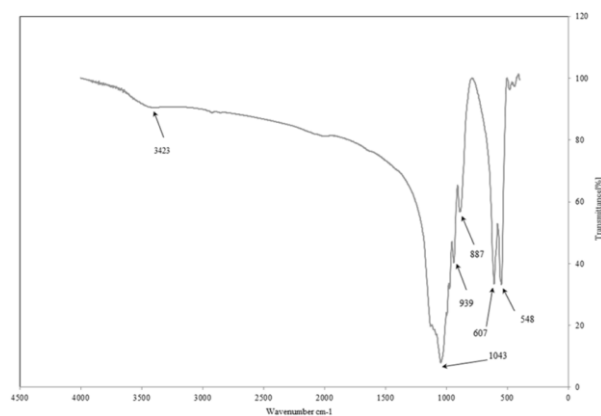
Figure 2. FT-IR pattern of MHAp heated at 1100°C

Fig. 3 indicates the FE-SEM pictures of magnetic hydroxyapatite powder heated at 500℃ and 1100℃. According to the pictures, the crystals of MHAp grow during the heating process. The results obtained from FE-SEM test were in agreement with those of the XRD test in Scherrer's method. The morphology of the particles in the (a) and (b) images are in the form of Irregular flat.
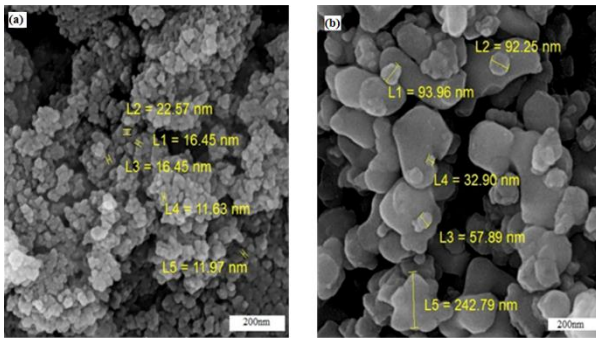
Figure 3. FE-SEM pictures of the MHAp powder heated at 500℃ (a) and 1100℃ (b)

3.2. Investigation of magnetic properties

The sample heated at 1100℃ was the main sample used for VSM test. According to Fig. 4 and its hysteresis loop, coercive field (H_c), saturation magnetization (M_s), and magnetism stayed (M_r) are 0.175 kO$_e$, 0.00147 emug^{-1}, and 0.02615 emug^{-1}, respectively, in -10 to 10 kO$_e$ magnetic field. Based on the obtained numbers and slope of the hysteresis curve, it can be concluded that the MHAp was characterized by a low magnetic property. The formation of low saturation magnetic field can be due to the interaction of diamagnetic reaction of hydroxyapatite with magnetite particles. In other words, applying a magnetic field to the MHAp powder creates an induced magnetic field in an opposite direction to the applied field in the structure, which can reduce the magnetic strength of the powder [24].
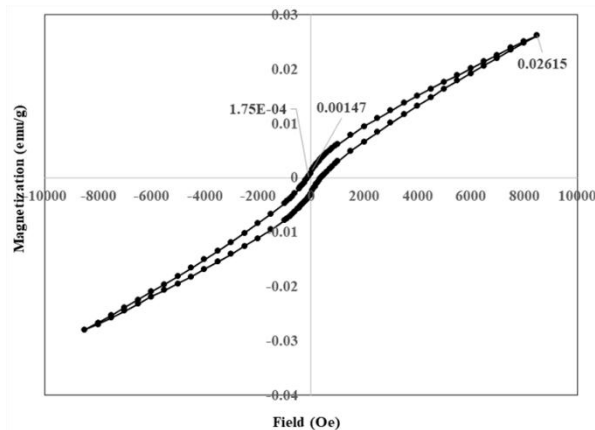
Figure 4. Hysteresis loop of MHAp heated in 1100℃ by VSM test

3.3. Investigation of grain growth

According to the results presented in Table 1, during heat treatment, nanoscale grain growth occurs. In general,

grain growth occurs in polycrystalline materials to decrease the free energy of the system by reducing the total grain boundary energy. The earliest consideration of kinetics of normal grain growth assumes a liner relation between the growth rate and the inverse of crystallite size [25, 26]:

$$\frac{dD}{dt} = \frac{k}{D} \tag{2}$$

where D, t, and k are the main grain diameter, heating time, and growth rate constant, respectively. The integration form of this equation is:

$$D^2 - D_0^2 = kt \tag{3}$$

And

$$k = k_0 exp\left(-\frac{Q}{RT}\right) \tag{4}$$

where R, Q, T, and k_0 are the universal gas constant, activation energy, absolute temperature, and a constant, respectively. Equations (3) and (4) are used for a simple investigation of the growth rate and activation energy of MHAp crystallites. Approximately, a single growth process can be separated as several domains where k is the constant for each domain [27]:

$$\int_{D_0}^{D_n} DdD = \int_{D_0}^{D_1} DdD + \cdots + \int_{D_{n-1}}^{D_n} DdD$$
$$= \int_{t_0}^{t_1} k_1 dt + \cdots + \int_{t_{n-1}}^{t_n} k_n dt \tag{5}$$

Or

$$D^2 - D_0^2$$
$$= \begin{cases} k_1 t & t \leq t_1 \\ \cdots & \cdots \\ k_1 t + \cdots + k_n(t_n - t_{n-1}) & t_n > t > t_{n-1} \end{cases} \tag{6}$$

k_1, k_2, …, and k_n are the growth rate constants in each domain. The values for k_1, k_2, and k_3 for n=3 were calculated in this study, the results of which are presented in Table 2 and Fig. 5. As mentioned earlier, the growth rate constants increase with time: $k_1 < k_2 < k_3$. The activation energy can be obtained from Equation (4) as the slope of a plot of (ln k) against (1/T). This plot is shown in Fig. 6 for the minor and major temperatures of every domain. The average activation energies for lower and higher temperatures are 45.51 and 67.33 kJ/mol, respectively.

TABLE 2. Constant growth rate in each domain

Time range [s]	Rate constant [nm^2/s]
3000-4200	0.1773
4200-5400	0.6106
5400-6600	2.0482
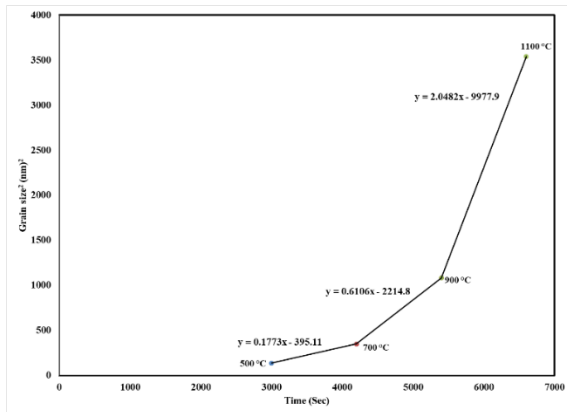
Figure 5. Growth curve based on time of MHAp for n=3 according to Equation 6
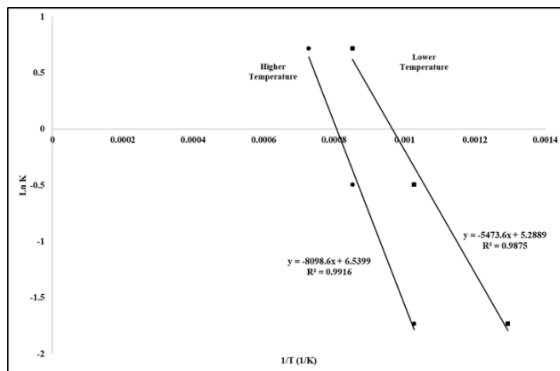
Figure 6. Arrhenius plot of logarithm of the rate constants versus reciprocal heat treatment temperature

Of note, for nanoscale materials, the grain growth was accompanied by a reduction in the diffusion rate and increase in the activation energy of diffusion [28]. It is unclear what happens in the growth process of MHAp during heat treatment. F. Liu and R. Kirchheim [29] introduced a new empirical relationship using the Gibbs adsorption equation and McLean model for grain boundary segregation. According to this approach, in systems with high segregation energy, decreasing the grain boundary energy to zero is possible. In addition, the decrease in the activation energy can be described

through this equation. The crystallite size is proportional to the inverse exponential part of temperature with in their relation [30]:

$$D = \frac{A}{B - exp\left(-\frac{C}{T}\right)} \qquad (7)$$

where A, B, and C are constant coefficients and T is temperature. Relationship (7) can present a better fitting for the MHAp growth profile. Of note, at high temperature (about 1673 K), the H and O atoms leave HAp crystalline lattice, and this defect in the lattice facilitates the formation of tricalcium phosphate. According to F. Liu and R. Kirchheim, the mobility of H and O atoms may increase at high temperatures, making the crystallites overcome the energy barrier at the grain boundary. This can be described as a "semi-segregation" phenomenon during heat treatment and explains changes in the rate constant and activation energy at high temperatures. It should be noted that the constants in the F. Liu and R. Kirchheim relation are not known for MHAp [30].

4. CONCLUSION

The VSM results showed that the synthesized MHAp had magnetic characteristics after heat treatment. In this study, the coercive field (H_c), saturation magnetization (M_s), and magnetism stayed (M_r) were 0.175 kOe, 0.00147 emug^{-1}, and 0.02615 emug^{-1}, respectively, in -10 to 10 kO$_e$ magnetic field. The growth kinetics of the magnetic HAp crystallite was also studied. The results revealed the growth activation energies of 45.51 and 67.33 kJ/mol for low- and high-temperature ranges, respectively. Due to the properties which has been proven eralier, the MHAp powder was successfully synthesized.

5. ACKNOWLEDGMENTS

REFERENCES

1.   Thanh, D. N., Novák, P., Vejpravova, J., Vu, H. N., Lederer, J., Munshi, T., "Removal of copper and nickel from water using nanocomposite of magnetic hydroxyapatite nanorods", *Journal*

of Magnetism and Magnetic Materials, Vol. 456, (2018), 451-460. https://doi.org/10.1016/j.jmmm.2017.11.064

2. Ramdani, A., Kadeche, A., Adjdir, M., Taleb, Z., Ikhou, D., Taleb, S., Deratani, A., "Lead and cadmium removal by adsorption process using hydroxyapatite porous materials", *Water Practice & Technology*, Vol. 15, No. 1, (2020), 130-141. https://doi.org/10.2166/wpt.2020.003

3. Wang, Y., Hu, L., Zhang, G., Yan, T., Yan, L., Wei, Q., Du, B., "Removal of Pb (II) and methylene blue from aqueous solution by magnetic hydroxyapatite-immobilized oxidized multi-walled carbon nanotubes", *Journal of Colloid and Interface Science*, Vol 494, (2017), 380-388. https://doi.org/10.1016/j.jcis.2017.01.105

4. Vahdat, A., Ghasemi, B., Yousefpour, M., "Synthesis of hydroxyapatite and hydroxyapatite/Fe_3O_4 nanocomposite for removal of heavy metals", *Environmental Nanotechnology, Monitoring & Management*, Vol 12, (2019), 100233-100238. https://doi.org/10.1016/j.enmm.2019.100233

5. Venkatesan, S., ul Hassan, M., Ryu, H. J., "Adsorption and immobilization of radioactive ionic-corrosion-products using magnetic hydroxyapatite and cold-sintering for nuclear waste management applications", *Journal of Nuclear Materials*, Vol 514, (2019), 40-49. https://doi.org/10.1016/j.jnucmat.2018.11.026

6. Mondal, S., Manivasagan, P., Bharathiraja, S., Moorthy, M. S., Kim, H. H., Seo, H., Lee, K. D., Oh, J., "Magnetic hydroxyapatite: a promising multifunctional platform for nanomedicine application", *International Journal of Nanomedicine*, Vol 12, (2017), 8389-8393. https://doi.org/10.2147/ijn.s147355

7. Zilm, M. E., Chen, L., Sharma, V., McDannald, A., Jain, M., Ramprasad, R., Wei, M., "Hydroxyapatite substituted by transition metals: experiment and theory", *Physical Chemistry Chemical Physics*, Vol 18, No. 24, (2016), 16457-16465. https://doi.org/10.1039/c6cp00474a

8. Orooji, Y., Mortazavi-Derazkola, S., Ghoreishi, S. M., Amiri, M., Salavati-Niasari, M., "Mesopourous Fe_3O_4@ SiO_2-hydroxyapatite nanocomposite: Green sonochemical synthesis using strawberry fruit extract as a capping agent, characterization and their application in sulfasalazine delivery and cytotoxicity", *Journal of Hazardous Materials*, Vol. 400, (2020), 123140. https://doi.org/10.1016/j.jhazmat.2020.123140

9. Katundi, D., Bayraktar, E., Gatamorta, F., Miskioglu, I., "Design of Hydroxyapatite/Magnetite (HAp/Fe_3O_4) Based Composites Reinforced with ZnO and MgO for Biomedical Applications", *BiomedIcal Journal of Scientific & Technical Research*, Vol 21, No. 4, (2019), 16113. https://doi.org/10.26717/bjstr.2019.21.003649

10. Zeng, D., Dai, Y., Zhang, Z., Wang, Y., Cao, X., Liu, Y., "Magnetic solid-phase extraction of U(VI) in aqueous solution by Fe_3O_4@hydroxyapatite", *Journal of Radioanalytical and Nuclear Chemistry*, Vol. 324, No. 3, (2020), 1329-1337. https://doi.org/10.1007/s10967-020-07148-y

11. Ain, Q. U., Zhang, H., Yaseen, M., Rasheed, U., Liu, K., Subhan, S., Tong, Z., "Facile fabrication of hydroxyapatite-magnetite-bentonite composite for efficient adsorption of Pb (II), Cd (II), and crystal violet from aqueous solution", *Journal of Cleaner Production*, Vol 247, (2020), 119088. https://doi.org/10.1016/j.jclepro.2019.119088

12. Das, K. C., Dhar, S. S., "Remarkable catalytic degradation of malachite green by zinc supported on hydroxyapatite encapsulated magnesium ferrite (Zn/HAP/$MgFe_2O_4$) magnetic novel nanocomposite", *Journal of Materials Science*, Vol 55, No. 11, (2020), 4592-4606. https://doi.org/10.1007/s10853-019-04294-x

13. Das, K. C., Das, B., Dhar, S. S., "Effective Catalytic Degradation of Organic Dyes by Nickel Supported on Hydroxyapatite-Encapsulated Cobalt Ferrite (Ni/HAP/$CoFe_2O_4$) Magnetic Novel

14. Nanocomposite", *Water, Air, & Soil Pollution*, Vol. 231, No. 2, (2020), 43. https://doi.org/10.1007/s11270-020-4409-1

14. Attia, M. A., Moussa, S. I., Sheha, R. R., Someda, H. H., Saad, E. A., "Hydroxyapatite/$NiFe_2O_4$ superparamagnetic composite: Facile synthesis and adsorption of rare elements", *Applied Radiation and Isotopes*, Vol. 145, (2019), 85-94. https://doi.org/10.1016/j.apradiso.2018.12.003

15. Seyfoori, A., Ebrahimi, S. S., Omidian, S., Naghib, S. M., "Multifunctional magnetic $ZnFe_2O_4$-hydroxyapatite nanocomposite particles for local anti-cancer drug delivery and bacterial infection inhibition: an in vitro study", *Journal of the Taiwan Institute of Chemical Engineers*, Vol. 96, (2019), 503-508. https://doi.org/10.1016/j.jtice.2018.10.018

16. Elkady, M., Shokry, H., Hamad, H., "Microwave-Assisted Synthesis of Magnetic Hydroxyapatite for Removal of Heavy Metals from Groundwater", *Chemical Engineering & Technology*, Vol. 41, No. 3, (2018), 553-562. https://doi.org/10.1002/ceat.201600631

17. Sneha, M., Sundaram, N. M., "Preparation and characterization of an iron oxide-hydroxyapatite nanocomposite for potential bone cancer therapy", *International Journal of Nanomedicine*, Vol 10, (2015), 99-105. https://doi.org/10.2147/ijn.s79985

18. Periyasamy, S., Gopalakannan, V., Viswanathan, N., "Hydrothermal assisted magnetic nano-hydroxyapatite encapsulated alginate beads for efficient Cr (VI) uptake from water", *Journal of Environmental Chemical Engineering*, Vol. 6, No. 1, (2018), 1443-1454. https://doi.org/10.1016/j.jece.2018.01.007

19. Cullity, B. D., *Elements of X-ray Diffraction*, 2nd Ed., edited by Morris Cohen, Addison-Wesley Publishing, (1977).

20. Younesi, M., Javadpour, S., Bahrololoom, M. E., "Effect of Heat Treatment Temperature on Chemical Compositions of Extracted Hydroxyapatite from Bovine Bone Ash", *Journal of Materials Engineering and Performance*, Vol 20, No. 8, (2011) 1484-1490. https://doi.org/10.1007/s11665-010-9785-z

21. Xia, X., Chen, J., Shen, J., Huang, D., Duan, P., Zou, G., "Synthesis of hollow structural hydroxyapatite with different morphologies using calcium carbonate as hard template", *Advanced Powder Technology*, Vol 29, No. 7, (2018), 1562-1570. https://doi.org/10.1016/j.apt.2018.03.021

22. Hamad, H. A., Abd El-latif, M. M., Kashyout, A. B., Sadik, W.A., Feteha, M.Y., "Study on synthesis of superparamagnetic spinel cobalt ferrite nanoparticles as layered double hydroxides by co-precipitation method", *Russian Journal of General Chemistry*, Vol. 84, No. 10, (2014), 2031–2036. https://doi.org/10.1134/s1070363214100296

23. Sneha, M., Sundaram, N. M., "Preparation and characterization of an iron oxide-hydroxyapatite nanocomposite for potential bone cancer therapy", *International Journal of Nanomedicine*, Vol 10, (2015), 99-106. https://doi.org/10.2147/ijn.s79985

24. Tien C., *Adsorption Calculations and Modeling*, *Butterworth-Heinemann publisher*: Boston, (1994). https://doi.org/10.1016/c2009-0-26911-x

25. Atkinson, H. V., "Overview no. 65: Theories of normal grain growth in pure single phase systems", *Acta Metallurgica*, Vol. 36, No. 3, (1988), 469-491. https://doi.org/10.1016/0001-6160(88)90079-x

26. Mobasherpour, I., Salahi, E., Manafi, S. A., Kamachali, R. D., "Effect of heat-treatment on grain growth of nanocrystalline tricalcium phosphate powder synthesized via the precipitation method", *Materials Science-Poland*, Vol. 29, No. 3, (2011), 203-208. https://doi.org/10.2478/s13536-011-0032-6

27. Liu, F., Kirchheim, R., "Comparison between kinetic and thermodynamic effects on grain growth", *Thin Solid Films*, Vol 466, No. 1-2, (2004), 108-113. https://doi.org/10.1016/j.tsf.2004.03.018

28. Höfler, H. J., Tao, R., Kim, L., Averback, R. S., Altstetter, C. J., "Mechanical properties of single-phase and nano-composite

metals and ceramics", *Nanostructured Materials*, Vol. 6, No. 5-8, (1995), 901-904. https://doi.org/10.1016/0965-9773(95)00205-7

29. Liu, F., Kirchheim, R., "Nano-scale grain growth inhibited by reducing grain boundary energy through solute segregration",

Journal of Crystal Growth, Vol 264, No. 1-3, (2004), 385-391. https://doi.org/10.1016/j.jcrysgro.2003.12.021

30. Mobasherpour, I. Salahi, E., "Effect of heat treatment on grain growth of nanocrystalline hydroxyapatite powder", *Journal of Ceramic Science and Technology*, Vol 2, No. 2, (2011), 119-124. https://doi.org/10.4416/JCST2010-00046

Advanced Ceramics Progress

Research Article

TiO₂-Coated Electrode for Plasma Dry Reformer for Synthesis Gas Production in Ambient Conditions

S. A. Mousavi [a], A. Irankhah [a] *, S. Beitlafteh [b]

[a] Hydrogen and Fuel Cell Research Laboratory, Chemical engineering Department, Faculty of Engineering, University of Kashan, Kashan, Isfahan, Iran

[b] School of Chemistry, The University of Manchester, Oxford Road, Manchester M13 9PL, England, United Kingdom

ARTICLE INFO

ABSTRACT

Conversion of methane to syngas via plasma technology is a cost-effective approach to obtaining syngas. Methane conversion by means of ceramic electrodes was significantly increased. In plasma reformer, while electrical discharge is available in gas, very active species such as electrons, radicals, ions, atoms, and excited molecules are produced and they function as catalysts. Methane and carbon dioxide gases at atmospheric temperature and pressure in the non-thermal with TiO₂-coated electrode plasma reactor with an inner diameter of 9 mm are converted to hydrogen and carbon monoxide (syngas) through one chemical step. The main objective of this research was to investigate the effects of changes in feed flow rate and feed ratio on methane conversion and product selectivity, as well as product distribution. Furthermore, the results were obtained when three synthesized catalysts were inserted in a section (3 mm) of plasma length (100 mm). The obtained results demonstrated that the voltage of 15 kV was required for methane conversion and hydrogen production. Reducing voltage and/or increasing the partial pressure ratio of methane to carbon monoxide in the reactor inlet resulted in the reduction of methane conversion rate. Moreover, according to the findings, increasing the ratio of carbon dioxide to methane would increase methane conversion and consequently, decrease the conversion of carbon dioxide. The conversion of methane and carbon dioxide was higher for co-precipitated Ce-Mn oxide support than those using the two other methods.

1. INTRODUCTION

Synthesis gas is a mixture of hydrogen and carbon monoxide and it is used functions as a primary material in the chemical industry (such as methanol synthesis, Fischer-Tropsch process, etc.) and food production. It is also used as the main energy carrier in fuel cells. Available processes including catalytic steam reforming, dry reforming, and partial oxidation at high temperatures require specific costly conditions to produce synthesis gas. Therefore, in order to reduce cost, energy, and time, non-thermal (cold) plasma is used [1, 2].

Among the different types of plasma, cold plasma creates an ideal tool for starting the reaction due to its non-equilibrium feature and availability of operating in atmospheric pressure and temperature. Cold plasma has been highly implemented by researchers due to its high reactivity and good performance at low temperatures. Applications of plasma include surface etching, fabrication, coating, air purification, ozone production, desulfurization, and plasma TVs [3].

Active plasma creation would lead to the formation of free radicals, ions, and excited molecules and in the desired process, the most significant result would be the formation of H₂ and CO gas molecules from mixtures of methane and carbon dioxide. Materials are divided into four categories in terms of phases including solid, liquid, gas, and plasma. The solid, liquid, and gas materials are

different in their adhesion forces of their constituent molecules. By heating solids or liquids, atoms with molecules obtain the heat energy they need to overcome the intermolecular adhesion force and become liquid or gas. If enough energy was given to the gas, the kinetic energy of the particles would increase. Due to the collision of particles whose kinetic energy was higher than the adhesion energy inside the molecules with gaseous particles, the gas molecules would gradually gain enough energy to overcome the intermolecular forces and be converted into their constituent atoms. At this point, if more energy is given to the gas, the gas atoms receive the energy required to overcome the forces holding the outermost electrons to become ionized gas or plasma. This conversion of gas to plasma is not a phase change, but only a transformation that occurs gradually with an increase in the temperature of the material (kinetic energy) [3, 4].

In some low-pressure conditions, the effect of the electromagnetic field on the motion of the particles in the plasma can be greater than that of the collision between the particles, hence forming the non-collision plasma. Given that ionization in plasma occurs due to the collision between the energetic electron particles and heavier ones, if plasma is generally viewed away from the charge accumulation regions, a high degree of freedom for the plasma environment can be achieved which is in fact the strength of the plasma [5, 6].

In other words, a system with high degrees of freedom and the most economical results obtained from using plasma reactors can be obtained with negatively charged natures, which are almost equal and because of this, plasma forms a quasi-neutral environment. The concept of plasma quasi-neutrality becomes clearer in correlation with the concepts of Debye protection and Debye length [5, 7].

Although plasma is electrically neutral, it incorporates both positive and negative particles. The same positive and negative particles create electric currents and subsequently, an electric field as they move; therefore, each particle is affected by the electric field of other particles. In this regard, the following steps should be noted.

1- Reduce the fixed investment costs;
2- Reduce the payback time;
3- Determine the flexibility of the operating unit to convert a wide range of hydrocarbons; and
4- Produce the synthetic gas at different CO/H_2 ratios and meet the feed needs of a wide range of petrochemicals [8, 9].

Table 1 briefly shows the previous research works based on the types of used plasma, power consumption, feed flow rates, and their results on methane and CO_2

conversions as well as hydrogen and carbon monoxide selectivity and the energy efficiency of a plasma reactor for gas conversion. Compared to DBD methods, power is observed to be more suitable and the rate of methane conversion with low energy consumption in this work is competitive with other works. The energy efficiency is defined in the following equation [9]:

$$E(mmol/kJ) = [CH_4 \text{ converted (mmol)} + CO_2 \text{ converted (mmol)}]/ \text{ Power (W)} \qquad (1)$$

Here, environmentally benign TiO_2 coating is prepared using a Physical Vapor Deposition (PVD) technique, allowing for an improvement in the efficiency of the electrode [10]. This study reports the methane conversion in plasma reactor with $TiO2$-coated electrode. The main objective of this study is to investigate the effect of the voltage, partial pressure change of argon and methane, and changes in the feed flow rate on methane conversion and product selectivity as well as product distribution and energy efficiency in an in-house manufactured plasma reactor with TiO_2-coated electrode.

2. EXPERIMENTAL PROCEDURE

2.1. Plasma methane reformer

In methane dry reforming, a comprehensive device was designed to produce hydrogen and carbon monoxide with cold plasma, the details of which are discussed in the following. For dry methane reforming and reactor test, argon, carbon dioxide, methane, and hydrogen gases with purity of 99.99% were used.

● **Transformers**

In this reactor, the minimum required voltage for methane dry reforming to produce syngas is 15 kV. To this end, a DC transformer was utilized. Due to the quite high voltage of the transformer outputs, the following points must be carefully observed:
a. If there is a transformer earth wire, the relevant wire must be connected to the standard earth and in transformers with earth wire, none of the outputs should be connected to the body. Any failure to do so would damage the transformer and reduce efficiency.
b. A radial distance of at least one centimeter is required for each of the transformer outputs relative to the other wires or any other metals. Therefore, it is not allowed to use clamps to connect the cables to each other or to the body.
c. The longer the length of the ignition wires, the higher the current drop and leakage, hence causing a severe reduction in the output power at the electrodes.
d. Special coated cables are used to connect the transformer to the electrode.

TABLE 1. Comparison of energy efficiency of dry reforming and different plasma sources

Plasma	Power (W)	Feed Flow (ml/ min)	Conversion (%)		Selectivity (%)		E (mmol/kJ)	Ref.
			CH₄	CO₂	H₂	CO		
DBD	50	50	56.4	30.2	31	52.4	0.32	[8]
DBD	500	500	40	20	-	88.5	0.18	[7]
DBD	100	60	64.3	43.1	-	32.2	0.26	[5]
Pulsed Corona	42	25	63.7	60.2	-	62.6	0.26	[6]
RF	30.6	100	31	24	100	20	0.68	[11]
RF	36.2	200	65.9	57.8	-	85.9	2.4	[12]
DC Corona	45	60	80	70	84	87	0.74	[13]
Plasma jet	69.85	2200	61	50	89.3	72.6	12.2	[14]
DBD	175	20	75	50	72	85	0.05	[15]
DBD	75	60	40	25	40	-	0.19	[16]
Pulsed DBD	12	22.5	30.1	20	32.1	44.4	0.13	[17]
Glaiding Arc	165	7500	13.1	8.4	31.4	69.5	3.1	[9]
C DBD	50	62	55.28	52.16	75.82	74.37	0.32	This work

● Reactor tests in quartz plasma reformer

The system employs three Brooks mass flow controllers to measure and control the gas flow rate in the range of 0 to 200 ml/min with high accuracy. This device is also able to read information by a computer. Prior to entering the reactor, a gas mixer is utilized. A quartz tubular reactor with an internal diameter of 9 mm in atmospheric conditions was used to perform reactor tests and determine plasma activity, as shown in Figure 1. The structure of this reactor consists of two electrodes. The applied electrodes in this reactor are made of stainless steel which is a rod electrode with an diameter of 1.5 mm inside the reactor coated with titanium oxide and a spiral electrode with a diameter of 1 mm outside the reactor. Inlet gases enter from the top of the reactor and after colliding with the plasma, a reforming reaction takes place. In some experiments, both catalyst and plasma are simultaneously used. The volume of the input feed has considerable effect on the reaction. The product is taken out of the bottom of the reactor and after passing through the cold trap, it is transferred to the gas chromatograph for further analysis. Exhaust gases from the reactor have some moisture. In order to liquefy the product gases, they are injected into the circulator and after leaving, this dry gas is transferred to the chromatograph and the components of the gas composition are determined.
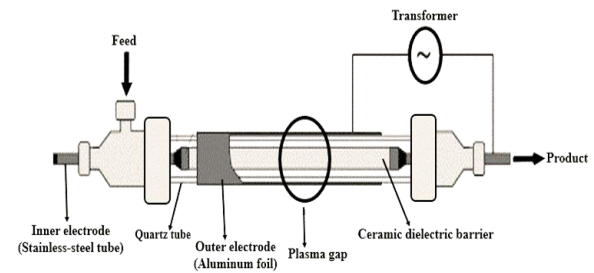
Figure 1. Plasma reformer by ceramic dielectric barrier

● Gas chromatograph

Shimadzu gas chromatography device was utilized to determine the feed composition and percentage of products. To analyze the products and feed input in the dry methane reforming process, a TCD detector with a filled Carbosieve column was used. To analyze the registered chromatograms, Chromanit software was also employed that could calculate the height and surface area below the peak and estimate the percentages of area and volume for each gas sample.

The circulator device was designed and built for cooling the cold trap and condensing the vapor products in reactor effluent based on the Carnot cycle. In this cycle, 134a refrigerant gas enters the condenser after leaving the compressor. After cooling, the gas flows to the evaporator to be cooled by the installed fan. The mechanical components include compressor, condenser, filter (dryer), capillary tube, and evaporator.

The conversion rates of methane and carbon dioxide as well as hydrogen and carbon monoxide yield were obtained from the following equations [8]:

$$\text{Methane conversion: } X_{CH_4} = \frac{CH_{4\,(in)} - CH_{4\,(out)}}{CH_{4\,(in)}} \times 100\% \quad (2)$$

$$\text{Carbon dioxide conversion: } X_{CO_{2\,(in)}} = \frac{CO_{2\,(in)} - CO_{2\,(out)}}{CO_{2\,(in)}} \times 100\% \quad (3)$$

$$\text{H}_2 \text{ yield: } \frac{H_{2\,(out)}}{2CH_{4\,(in)}} \times 100\% \quad (4)$$

$$\text{CO selectivity: } \frac{CO_{(out)}}{CH_{4\,(in)} + CO_{2\,(in)}} \times 100\% \quad (5)$$

2.2. TiO₂ ceramic dielectric barrier

Commercial titanium dioxide nanoparticles were purchased from Degussa Korea (Incheon, Korea). The PVD parameters are as follows: a working pressure of 7×10^3 Torr, an RF sputtering power of 200W, a deposition time of 180 min, and a bias voltage of -140 V.

Figures shows a cross-sectional SEM image of the TiO^2 coated, indicating the formation of thin (1.2 μm) and compact coating layers which homogeneously cover the surface of the electrode. Figure 2 shows the Scanning Electronic Microscopy (SEM) images of TiO_2 nanoparticles at different scales and surfaces of electrodes coated with TiO_2 nanoparticles. As shown in Figure 2, nanoparticles have good uniformity hence a suitable and acceptable function as a dielectric barrier.
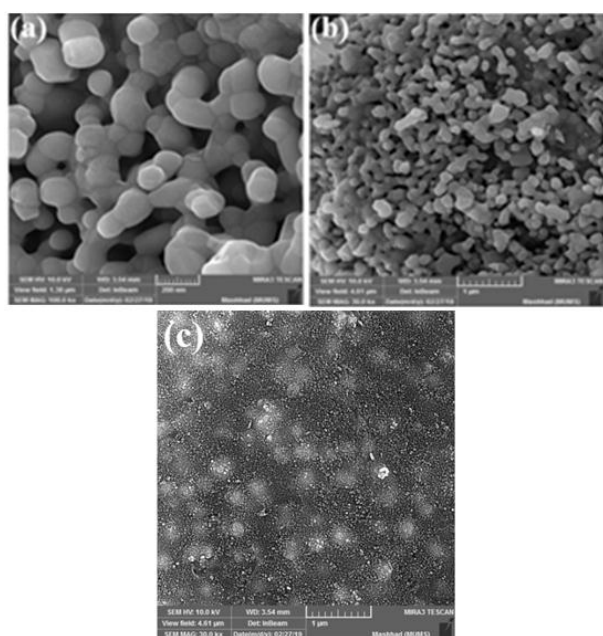

Figure 2. SEM image of TiO_2 nanoparticles on different scales (a) 200 nm (b) 1 μm (c) Surface of electrode coated with TiO_2 nanoparticles

3. RESULTS AND DISCUSSION

The results in Figs. (3-4) show that with an increase in the ratio of CO_2 to CH_4 from 0.5 to 3, methane and carbon dioxide conversion rates would increase and decrease, respectively. In addition, with an increase in CO_2/CH_4, a decrease in the H_2/CO ratio was observed mainly due to the effect of the reverse side reaction of water-gas shift, which is generally more at low CO_2/CH_4 ratios. At high CH_4/CO_2 ratios and temperatures, high methane conversion from the main dry reforming reaction could reduce the amount of sedimentary carbon generally obtained from methane decomposition; however, at a CH_4/CO_2 ratio higher than 1, due to adverse reactions such as reverse Bodouard reaction and reverse water-gas displacement, H_2/CO ratio would decrease. To ensure an

H_2/CO ratio close to 1, the CH_4/CO_2 ratio should be set to less than 1.
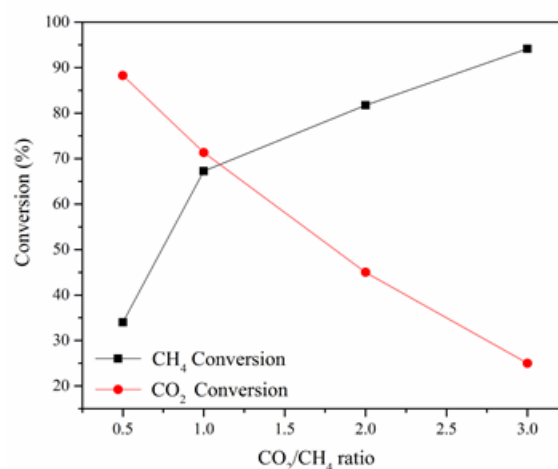

**Figure 3.** Effect of feed ratio on methane carbon dioxide and conversion
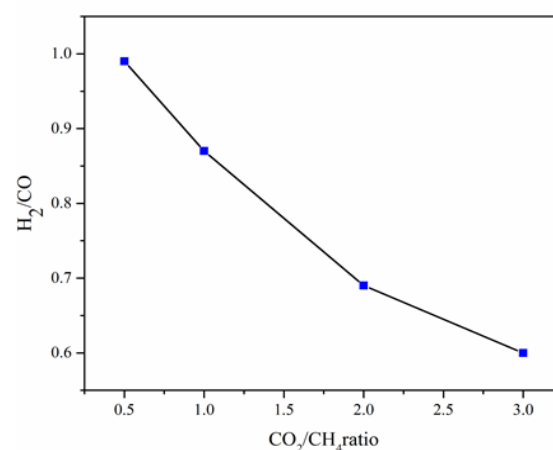
Figure 4. The effect of feed ratio on H_2/CO ratio

Of note, the desired results were obtained when three synthesized catalysts were inserted in a section of 3 mm with a plasma length of 100 mm. Figure 5 (a and b) shows the results of the stability test, i.e., CO_2 and CH_4 conversions versus time on stream for plasma reaction in the presence of nickel (10% wt.) supported on $Ce_{0.95}Mn_{0.05}O_2$ catalysts by means of (a) sol-gel, (b) co-precipitation, and (c) hydrothermal methods. As observed in these figures, the plasma environment can produce syngas for a long time and no noticeable decrease is observed in the performance of the reformer. The co-precipitated catalyst support has more activity than the two other method synthesized supports.
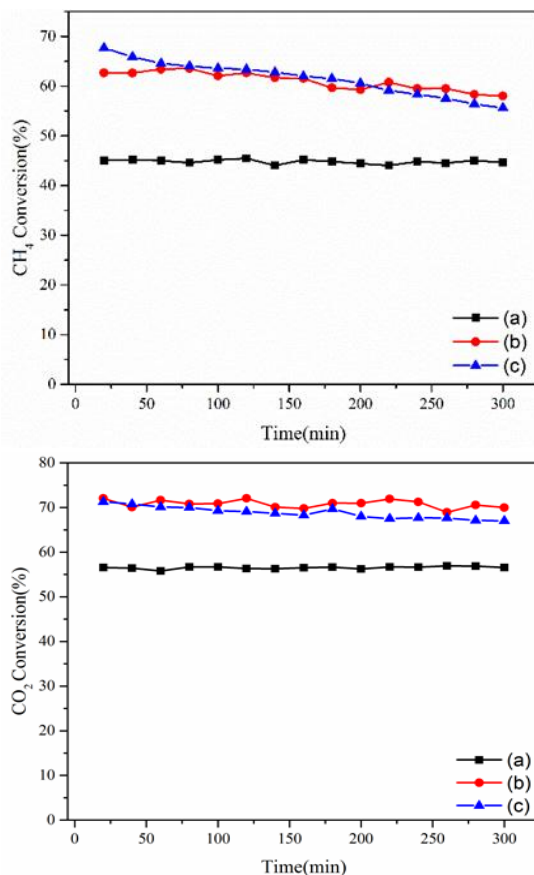
Figure 5. Conversion rate of methane and carbon dioxide for plasma assisted with $10Ni / Ce_{.95}Mn_{.05}O_2$ catalyst synthesized by (a) sol-gel, (b) co-precipitation, and (c) hydrothermal methods

As shown in Figure 6, the results of CH_4 conversion are compared in the presence and absence of TiO_2 coating on the electrode. The results show that coating the electrode with TiO_2 would increase the conversion of CH_4 to a desirable amount.
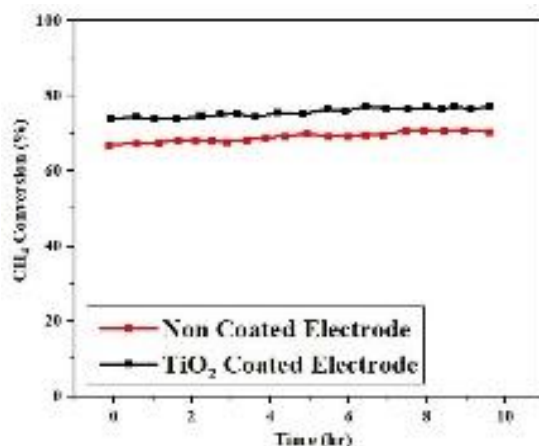
Figure 6. Time on stream for methane conversion

4. CONCLUSION

The present study investigated the dry reforming of methane with plasma. Numerous technologies have been used so far to convert methane as the main constituent of natural gas. The obtained results indicated that a 15 kV voltage was required for methane conversion and hydrogen production. Reducing the voltage and/or increasing the partial pressure ratio of methane to carbon monoxide in the reactor inlet led to a reduction in the rate of methane conversion. According to the findings, increasing the ratio of carbon dioxide to methane would increase methane conversion and decrease the carbon dioxide conversion. Given the structural properties and the results obtained from the catalytic activity of the samples, it can be concluded that the catalyst prepared by the co-precipitation method outperformed other samples. The rates of methane and carbon dioxide conversion were higher for co-precipitated Ce-Mn oxide support than those of the two other methods.

ACKNOWLEDGEMENT

REFERENCES

1. Wang, Q., Spasova, B., Hessel, V., Kolb, G., "Methane reforming in a small-scaled plasma reactor–Industrial application of a plasma process from the viewpoint of the environmental profile", *Chemical Engineering Journal*, Vol. 262, (2015), 766-774. https://doi.org/10.1016/j.cej.2014.09.091

2. Shavelkina, M. B., Ivanov, P. P., Bocharov, A. N., Amirov, R. K., "Numerical and Experimental Study of the Multichannel Nature of the Synthesis of Carbon Nanostructures in DC Plasma Jets", *Plasma Chemistry and Plasma Processing*, (2020), 1-19. https://doi.org/10.1007/s11090-020-10133-8

3. Bromberg, L., Cohn, D. R., Rabinovich, A., Alexeev, N., "Plasma catalytic reforming of methane", *International Journal of Hydrogen Energy*, Vol. 24, No. 12, (1999), 1131-1137. https://doi.org/10.2172/305623

4. Arcotumapathy, V., Vo, D. V. N., Chesterfield, D., Tin, C. T., Siahvashi, A., Lucien, F. P., Adesina, A. A., "Catalyst design for methane steam reforming", *Applied Catalysis A: General*, Vol. 479, (2014), 87-102. https://doi.org/10.1016/j.apcata.2014.04.020

5. Zhang, Y. P., Li, Y., Wang, Y., Liu, C. J., Eliasson, B., "Plasma methane conversion in the presence of carbon dioxide using dielectric-barrier discharges", *Fuel Processing Technology*, Vol. 83, No. 1-3, (2003), 101-109. https://doi.org/10.1016/s0378-3820(03)00061-4

6. Bin, D., Xiu-ling, Z., Wei-min, G., Ren, H., "Study on the methane coupling under pulse corona plasma by using CO_2 as

oxidant", ***Plasma Science and Technology***, Vol. 2, No. 6, (2000), 577. https://doi.org/10.1088/1009-0630/2/6/011

7. Zhou, L. M., Xue, B., Kogelschatz, U., Eliasson, B., "Nonequilibrium plasma reforming of greenhouse gases to synthesis gas", ***Energy & Fuels***, Vol. 12, No. 6, (1998), 1191-1199. https://doi.org/10.1021/ef980044h

8. Tu, X., Whitehead, J. C., "Plasma-catalytic dry reforming of methane in an atmospheric dielectric barrier discharge: Understanding the synergistic effect at low temperature", ***Applied Catalysis B: Environmental***, Vol. 125, (2012), 439-448. https://doi.org/10.1016/j.apcatb.2012.06.006

9. Tu, X., Whitehead, J. C., "Plasma dry reforming of methane in an atmospheric pressure AC gliding arc discharge: Co-generation of syngas and carbon nanomaterials", ***International Journal of Hydrogen Energy***, Vol. 39, No. 18, (2014), 9658-9669. https://doi.org/10.1016/j.ijhydene.2014.04.073

10. Tao, T., Bae, I. T., Woodruff, K. B., Sauer, K., Cho, J., "Hydrothermally-grown nanostructured anatase TiO2 coatings tailored for photocatalytic and antibacterial properties", ***Ceramics International***, Vol. 45, No. 17, (2019), 23216-23224. https://doi.org/10.1016/j.ceramint.2019.08.017

11. Yao, S. L., Ouyang, F., Nakayama, A., Suzuki, E., Okumoto, M., Mizuno, A., "Oxidative coupling and reforming of methane with carbon dioxide using a high-frequency pulsed plasma", ***Energy & Fuels***, Vol. 14, No. 4, (2000), 910-914. https://doi.org/10.1021/ef000016a

12. Yao, S. L., Okumoto, M., Nakayama, A., Suzuki, E., "Plasma reforming and coupling of methane with carbon dioxide", ***Energy & Fuels***, Vol. 15, No. 5, (2001), 1295-1299. https://doi.org/10.1021/ef010089+

13. Li, M. W., Xu, G. H., Tian, Y. L., Chen, L., Fu, H. F., "Carbon dioxide reforming of methane using DC corona discharge plasma reaction", ***The Journal of Physical Chemistry A***, Vol. 108, No. 10, (2004), 1687-1693. https://doi.org/10.1021/jp037008q

14. Li, D., Li, X., Bai, M., Tao, X., Shang, S., Dai, X., Yin, Y., "CO_2 reforming of CH_4 by atmospheric pressure glow discharge plasma: a high conversion ability", ***International Journal of Hydrogen Energy***, Vol. 34, No. 1, (2009), 308-313. https://doi.org/10.1016/j.ijhydene.2008.10.053

15. Wang, Q., Yan, B. H., Jin, Y., Cheng, Y., "Dry reforming of methane in a dielectric barrier discharge reactor with Ni/Al_2O_3 catalyst: interaction of catalyst and plasma", ***Energy & Fuels***, Vol. 23, No. 8, (2009), 4196-4201. https://doi.org/10.1021/ef900286j

16. Zhang, A. J., Zhu, A. M., Guo, J., Xu, Y., Shi, C., "Conversion of greenhouse gases into syngas via combined effects of discharge activation and catalysis", ***Chemical Engineering Journal***, Vol. 156, No. 3, (2010), 601-606. https://doi.org/10.1016/j.cej.2009.04.069

17. Goujard, V., Tatibouët, J. M., Batiot-Dupeyrat, C., "Use of a non-thermal plasma for the production of synthesis gas from biogas", ***Applied Catalysis A: General***, Vol. 353, No. 2, (2009), 228-235. https://doi.org/10.1016/j.apcata.2008.10.050

Advanced Ceramics Progress

Journal Homepage: www.acerp.ir

Lithium Substitution Glass Composition Used in Glass Ionomer Cement: Physiochemical Properties in Artificial Saliva

T. Mohammadi Hafshejani [a], A. Zamanian [a], A. Faeghinia [b] *

[a] Department of Nanotechnology and Advance Materials, Materials and Energy Research Center, Meshkindasht, Alborz, Iran
[b] Department of Ceramic, Materials and Energy Research Center, Meshkindasht, Alborz, Iran

A B S T R A C T

In this study, glasses with 41.6 SiO_2, 28.5 Al_2O_3, 15.5 CaF_2, 3.7 $AlPO_4$, 1.5 $AlF3$, (9.2-X) NaF, and X LiF (X= 0, 3, 6, and 9.2) compositions were prepared. Fourier Transform Infrared Spectroscopy (FTIR) showed the red shift of Si-O-Si vibration mode by Lithium substitutions. According to the results of Differential Thermal Analysis (DTA), $\Delta T_g = 60$ °C was proved by the lithium substitution. Field Emission Scanning Electron Microscopy (FESEM), antibacterial property, glass solubility in Artificial Saliva (AS), and pH variation in AS by dissolution were measured. Following the initial substitution of lithium, the glass density was reduced from 2.62 to 2.40 g/cm^3, whereas in the 6 wt. % Li concentration, the high field strength played the main role and the density increased from 2.40 to 2.58 g/cm^3. In artificial saliva with basic pH, the durability of Li bearing glasses increased and the degradation rate decreased. Durability decreased in the acidic environment. By increasing the Li substitution, the antimicrobial property of the cement was enhanced.

1. INTRODUCTION

Glass Ionomer Cements (GICs) have drawn considerable interest by those specializing in the field of dentistry over the last 50 years [1]. GICs are used in restorative dentistry as the filling materials, luting, and lining cements [2, 3]. A contributing factor is fluoride ion release. Fluoride prevents cavity progression and helps maintain adequate physical properties for chewing [3].

Additional factors include the low thermal expansion coefficient similar to the tooth structure which gives rise to the thermal compatibility of this glass with the tooth enamel. The setting reaction has low exothermic energy and GICs chemically bond with enamel and dentin. Close module coefficient with dentin, biocompatibility, and low cytotoxicity all play significant roles [4]. They are usually used in pediatric dentistry as filling, especially when micro-invasive approaches are selected instead of conventional methods for fixing the dental caries [5].

GICs are formed by mixing glass powder made of acid degradable fluoro-aluminosilicate and an ionomer with carboxylic acids, usually polyacrylic acid and copolymers of polyacrylicacid. In addition, they are formed with the reaction of liquid polyacid ionomer and the calcium released glass (forming insoluble polysalts) [5].

The decomposition of glass network by acid attack causes the release of aluminum and calcium from the outer layer of filler particles and it determines the crosslinking degree of the poly salt matrix [6-8]. Alkali metals are the main components of the powder, reduce the melting temperature, and form Non-Bridging Oxygens (NBOs) in the cement matrix as network modifiers [9, 10]. Incorporation of sodium in the glasses has diverse effect on some mechanical and physical properties [11]. When glass is under acid attack since Na^+ is more susceptible (less resistant or weaker) against acid

* Corresponding Author Email: a.faeghinia@merc.ac.ir (A. Faeghinia)

attack, Na^+ competes with Ca^{2+} and Al^{3+} in carboxylate groups [12].

Therefore, in view of all the factors considered, it can be concluded that the numbers and concentration of sodium ions should be low for cements.

It has been asserted that internal cracks and air bubbles in these cements cause micro-leakage [13-15]. Several strains of oral streptococci and bacteria, which can penetrate by micro-leakage, may lead to the dental plaque biofilms formation and thus, play a major role in the development of caries [16-19].

Lithium is an antibacterial metal and its antiviral and anti-parasitic properties have been previously shown [20-26]. It has been demonstrated that bioactivity in bio glass was increased by significant lithium addition [27]. Wang et al. developed the bio glass (55% Si_2O- 36% CaO- 4% P_2O_5- 5 Li_2O) with 5 wt.% Lithium with positive effect on mesenchyme cell proliferation and improved the antibacterial properties [28]. Further, it was stated that by using lithium carbonate, the bone mass would be increased [29]. In addition, the small molar weight of this ion reduced the density and solubility of glass in water [30-31].

However, the LiF effect on glass density, characteristic temperatures, glass structure, and finally acidic and basic resistance of GIC powder have not been studied before. In this work, the effect of substitution of NaF with different LiF concentrations on antibacterial properties and degradation of formed cements in acidic and basic environments is evaluated, which to the best of the authors' knowledge, the pH of environment has not been studied from the viewpoint of antibacterial properties before.

2. MATERIALS AND METHODS

2.1. Glass Synthesis

Four series of glass compositions based on 41.6 SiO_2, 28.5 Al_2O_3, 1.5 AlF_3, 3.7 $AlPO_4$, 15.5 CaF_2, (9.2-X) NaF, and X LiF were prepared with X= (0, 3, 6, and 9.2) and the samples were denoted by G1, G2, G3, and G4, respectively. The details of chemical composition of glasses are given in Table 1.

TABLE 1. Glass Composition

Sample Code	Content of components, Wt.%						
	SiO_2	Al_2O_3	$AlPO_4$	AlF_3	CaF_2	NaF	LiF
G_1	41.6	28.5	3.7	1.5	15.5	9.2	-
G_2	41.6	28.5	3.7	1.5	15.5	6.2	3
G_3	41.6	28.5	3.7	1.5	15.5	3.2	6
G_4	41.6	28.5	3.7	1.5	15.5	-	9.2

The batches were melted in alumina crucibles at 1350-1550 °C for 2 h (heating rate: 10 °C/min). The dried frits were ground and sieved so that the appropriate particle size <35 μm could be determined.

2.2. Glass Characterization
2.2.1. X-ray Diffraction

The crystalline/amorphous state of the samples was analyzed by X-Ray powder Diffraction (XRD). The X-ray patterns were obtained using a Scintag X-ray diffraction spectrometer (XRD, Philips- PW3710, The Netherlands) with Cu (Kα), operating nickel filtered Cu Kα radiation in the range of 2θ = 10° - 80°.

2.2.2. Fourier Transform Infrared Spectroscopy

The Fourier Transform Infrared (FTIR) spectra (Spectrum RXI, USA) of the glasses were recorded in the range of 400 – 4000 cm^{-1} with a spectral resolution of 2 cm^{-1}. The pellets with 13 mm diameter were prepared by mixing 10 mg of each sample with 1000 mg of KBr. The spectrum of each sample represents an average of 20 scans, which were normalized to the spectrum of blank KBr pellet.

2.2.3. Differential Thermal Analysis (DTA)

The thermal behavior of glasses was measured by differential thermal analysis (STA 409 PC Luxxto, Netzsch-Gerätebau GmbH Germany). The samples were tested in a condition in which the air is flowing with an alumina crucible and heated up to 1000 ℃ with a heating rate of 10 ℃ /min.

2.2.4. Density Measurement

The true density of the glasses was measured by means of a pycnometer (Accupyc 1330 pycnometer, Micrometrics Instruments, Norcross, Georgia, USA) using helium gas that produced the structural (true) density.

2.2.5. Glass Solubility

In this method, 150 mg of each glass was weighed and then, immersed in 100 mL of Artificial Saliva (AS) with 3.5, 6.8, and 9.2 pH. The composition of AS solution was made according to the instructions from [31]: 100 mL of KH_2PO_4 (2.5 mM); 100 mL of Na_2HPO_4 (2.4 mM); 100 mL $KHCO_3$ (1.50 mM); 100 mL of NaCl (1.0 Mm); 100 mL of $MgCl_2$ (0.15 mM); 100 mL of $CaCl_2$ (1.5 mM); and 6 mL of citric acid (0.002 mM). All specimens were incubated at 37 °C. Following different immersion time interval, the samples were removed and the weight of each remaining powder was recorded as m_2. The mass change during storage in artificial saliva was calculated by:

$$M_g = (m_1 - m_{2(t)})/m_1 \times 100 \tag{1}$$

During reactivity tests in different AS, pH changes were also assessed by a pH-meter (Aldrich-Z654280, Mettler Toledo, GmbH, Seven Easy pH meter).

2.2.6. Particles Morphology Analysis

Particle morphology of glass containing 9.2% Li was measured by Field Emission Scanning Electron Microscopy (FESEM Zeiss-DSM950,Oberkochen, Germany) operating at 25 kV before and after soaking in artificial saliva at pH=9.5 for 14 days.

2.3. Antibacterial Activity

For antibacterial testing by Colony Form Units (CFU) method, samples were incubated with the suspension of S.mutans at (1.5×108) CFU. The antibacterial activity was conducted by the plate-counting method. A phosphate buffer solution (pH ~ 7.4) containing the bacteria was used. The sample-containing solutions were incubated at 37 °C under vibration agitation for up to 24 h. Some of the solutions were then cultured on Brain Heart Infusion (BHI) and incubated at 37 °C for additional 24 hr, and the exact number of discrete colonies was counted as the number of the remaining bacteria. Antibacterial activity (E) was calculated through the following equation:

$$E(\%)=[(A-B)/A]\times100\% \qquad (2)$$

where A= number of viable bacteria with control glass (G1) in the tray and B=number of viable bacteria with lithium bearing glasses in the tray.

2.4. Cellular Behavior

MTT (3-dimethylthiazol-2, 5-diphenyltetrazolium bromide) colorimetric assay was used for determining cytotoxicity of samples. Briefly, disc-shaped cement samples with 1.00 mm thickness and 10 mm diameter were prepared. The samples were washed by ultrasonification with sterile distilled water and kept in sterilized appropriate flasks after disinfecting under ultraviolet light. Cytotoxicity tests were performed with the human osteoblast (G-292) cells. Cells were seeds at density of 1.5×10^4 cell/mL in a 96-well plate containing RPMI culture medium with 10% FBS and 1% Pen Sterp antibiotic. Then, the culture medium was discarded and the media supplemented with cements extracts were added to each cell and diluted by factors of 2, 4, and 8 with standard culture medium. After 24 h of incubation of the cells with the extracts, the media were exchanged with 100 μL of conditioned culture media containing 10% MTT solution and kept for 4 h. Then, cultural media were removed and 100 μL of dimethyl sulfoxide (DMSO) was added for dissolving the resulting formazon. The absorbance was read at 570 nm using a micro plate reader (BIO-TEK Elx 808, Highland park,

USA). The obtained values were expressed as a percentage of the control cells to which no discs were added. All tests were repeated three times.

2.5. Statistical Analysis

All experiments for determining antibacterial activity were performed in three replicates. Statistical analysis of the antibacterial activity was used by one-way ANOVA and Tukey tests. Also, the variation in pH and mass change data were analyzed by ANOVA. The $P<0.05$ level was considered statistically significant.

3. RESULTS AND DISCUSSION

The XRD patterns of amorphous phases with the control sample with similar patterns are presented in Figure 1.
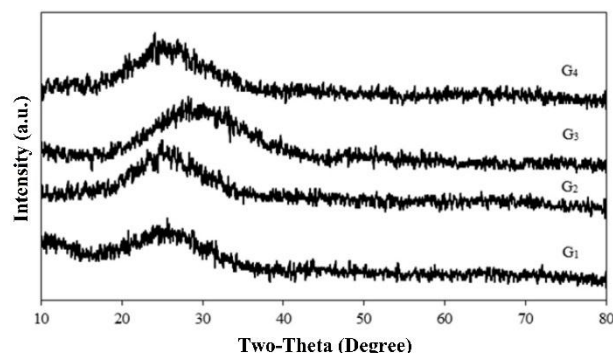

Figure 1. X-ray diffraction pattern of glass samples

The FTIR spectra of samples are illustrated in Figure 2. The high-frequency region, 800-1200 cm^{-1}, belongs to the asymmetric stretching mode of Si-O-Si. The frequency increases with the alkali compositions, suggesting greater stabilization with more efficient packing around Si-O-Si units, arising from an optimal mixing of Li$^+$ and Na$^+$ ions (G2 and G3). This could be confirmed by T_g results as well.
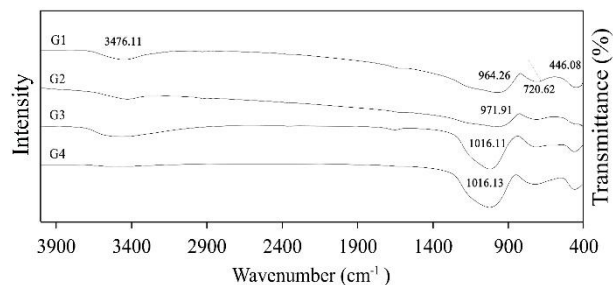

Figure 2. FTIR spectra of the investigated glasses

The peaks located at roughly 720 cm^{-1} are assigned to the Si-O-Si bridging oxygen atoms between the tetrahedra stretching [32], which have not changed clearly. Bands at 400-500 cm^{-1} could be attributed to the vibration of Si-O-Si and Al-O-Al [32]. Moreover, the weak bands at wave number 450 cm^{-1} might be associated with the vibration of the Li$^+$ cations [20].

Figure 3 shows the DTA results of glasses (G1, G2, G3, and G4). By the substitution of LiF to NaF composition, the T$_g$ peaks shift to the higher temperatures.
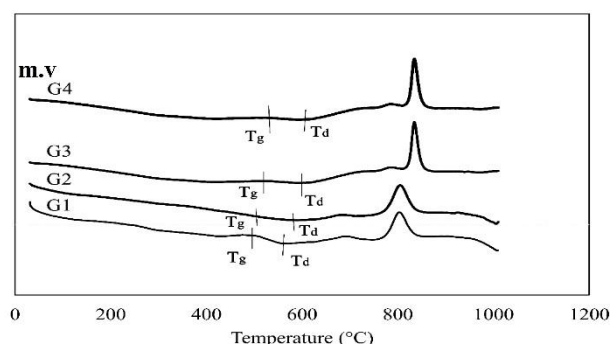
Figure 3. DTA curves samples (a):G1, (b):G2, (c):G3, and (d):G4

The transition temperatures, T$_g$ (G4: 594ºC, G3: 588ºC, G2: 570ºC, and G1: 530ºC) and softening tempertures, T$_d$ (G4: 627ºC, G3: 608ºC, G2: 592ºC, and G1: 570ºC) of the glasses shift to the higher temperatures by the substitution of Li. Moreover, the crystallization temperatures shift to the higher temperatures, too. The main reasons could be related to the breaking of the silicate glasses network in the presence of Na, which is easier than Li [33].

Since Li$^+$ ions have smaller radii than Na$^+$ and higher field strength of 1.65 than Na$^+$ ions, the glasses become more compact upon the substitution of NaF with LiF (Althought the viscosity of glasses was supposed to be decreased).

Table 2 shows that G3 has higher density than G2 and G4.

As is well known, two main factors influence the density of a glass: the molecule weight of glass components and the other is the compactness of glass network. The decreases in density of glasses with the intial substitutions can be ascribed to the lower molecule weight of LiF. The increased density can be discribed by the high field strength of Li$^+$, resulting in a stronger link between glass structure and the compacted structure.

Due to the field strength of lithium ion, the lithium-oxygen bond in G3 is stronger than sodium-oxygen bond in G1. However, with further Li substitution (G4), the low atomic weight of Li causes decreased density. Thus, the results depend on the concentration of lithium. The

atomic weight or strength field of this ion is the dominant factor.

It can be mentioned that the positive and negative effects of the substitutes on the glass structure are competing and non-monotonic changes in the glass properties with the substitutions are observed.

TABLE 2. Different densites obtained from glasses

| Sample Code	Density (g/cm^3)
G$_1$	2.62±0.02
G$_2$	2.47±0.05
G$_3$	2.58±0.05
G$_4$	2.40±0.01

Colony count method was used for the determination of antimicrobial activity. The antibacterial effect was reported quantitatively after close contact of cements with the S.mutans suspension. To ensure the reliability of this experiment, three samples were used for each cement. Based on the results, G4 showed a comparably greater antibacterial effect than G1 and it correlated with the lithium amount as compared to the other samples. Thus, the greatest degree of the cement's antibacterial activity is directly related to the lithium amount. The greatest inhibition of S.mutans growth depends on the high level release of the antibacterial agent from the cements; therefore, with further time interval, the antibacterial activity increased, too. Also, lithium was released steadily and, therefore, the antibacterial activity was durable and time dependent.

According to Figure 4, the antibacterial activities were effectively enhanced by the concentrations of the added disinfectant (p<0.05). G4 exhibits the highest value (99.17 %.) of antibacterial activity.

Figure 4 and Table 3 show that the greatest inhibition of S.mutans growth depends on the high level release of antibacterial agents from the glass.

Figure 5 shows that the mechanism of glass dissolution depends on the pH of environment. At an acidic pH, an ion exchanging between network modifiers in the bulk of the glass and the protons in the solution is the main reaction.

Figure 6 shows the pH of immersed glasses in the AS at immersion time. The differences between the soaked samples in AS at pH=3.5 and 6.8 were statistically significant (P<0.05). Increase rates of pH 6.8 and 3.5 at the initial time of immersion were followed by constant pH, indicating a reduced dissolution rate.
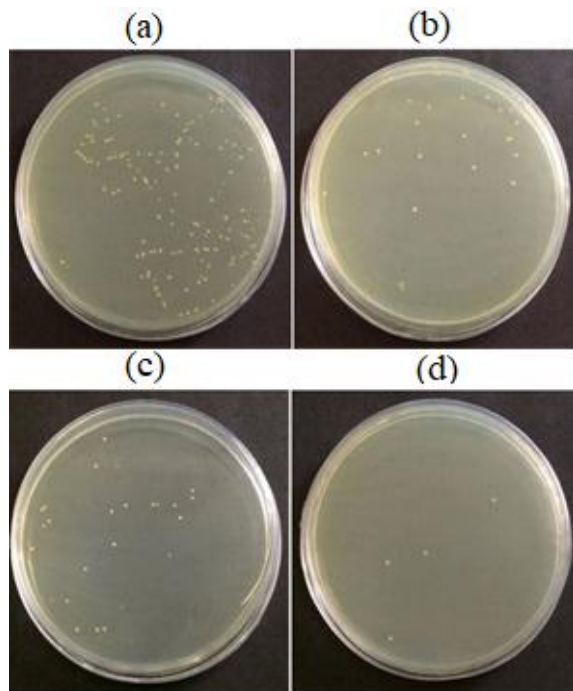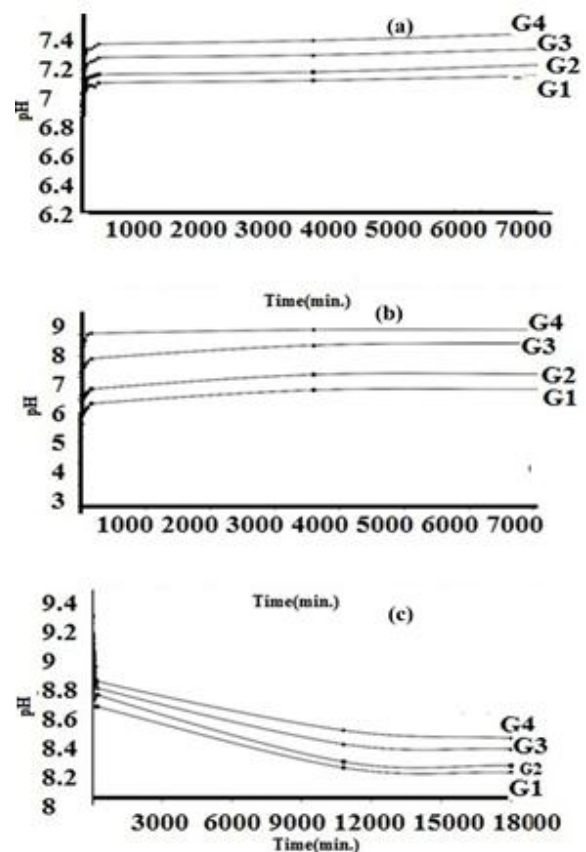
Figure 4. Actual images of the incubated (a, b, c, and d) S.mutans with G1, G2, G3 and G4, respectively.

TABLE 3. The results of S. mutans bacteria colonies

Sample	CFU/ml (start)	CFU/ml (after 24 h)	Antibacterial activity
G1	1.5×10^8	1.2×10^8	20
G2	1.5×10^8	2×10^6	83.33
G3	1.5×10^8	1.5×10^6	87.5
G4	1.5×10^8	1×10^5	99.17
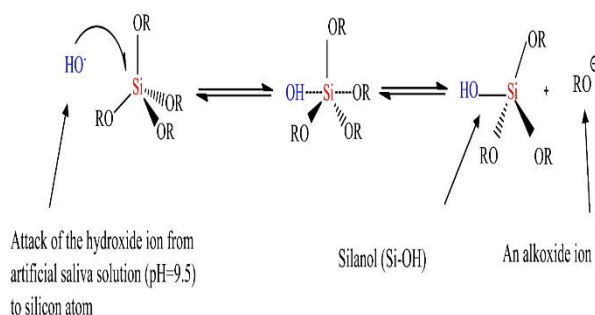
Figure 5. Scheme of dissolution of glass after soaking in basic artificial saliva

Figure 6. Changes in pH AS solutions after immersion of samples and their insets over initial 2 hours: (a) at pH = 6.8, (b) at pH = 3.5, and (c) at pH = 9.5

Figure 7 shows the formation of silanol groups (Si-OH) on the glass surface caused by ion exchanging.

In Figure 6, the reason for the initial increase in the pH of solutions is the cation exchanges of Ca^{2+}, Na^+, and Li^+ with H^+ from the solution. Therefore, after the glass immersion in the AS, the pH raises by the following ion exchange reactions and the OH^- concentration will be increased [33].

1) $Si\text{-}O\text{-}Na^+ + H^+ + OH^- \longrightarrow Si\text{-}OH + Na^+ (aq.) + OH^-$
2) $Si\text{-}O\text{-}Li^+ + H^+ + OH^- \longrightarrow Si\text{-}OH + Li^+ (aq.) + OH^-$
3) $Si\text{-}O\text{-}Ca^{2+} + H^+ + OH^- \longrightarrow Si\text{-}OH + Ca^{2+} (aq.) + OH^-$
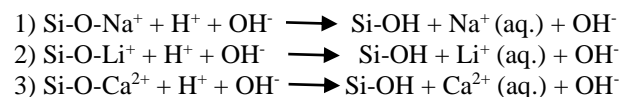
As the data illustrates, the increase of pH is in order G4>G3>G2>G1, pointing to the fact that fast ion exchanging occurred between $Li^+\text{-}H^+$ in the solution compared to $Na^+\text{-}H^+$ [34].
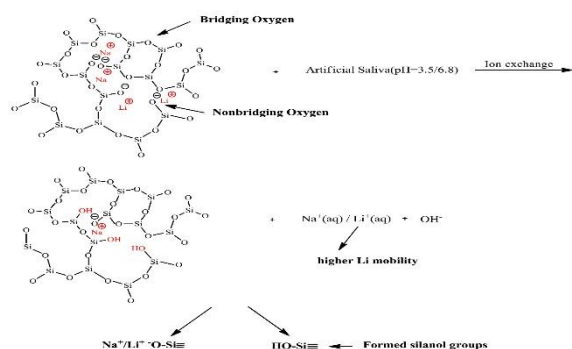
Figure 7. Mechanism of glass degradation after immersion in acidic artificial saliva

Figure 8. Mass change (Mg%) of glasses immersed in artificial saliva with different pHs over one month: (a) pH = 6.5, (b) pH = 3.5, and (c) pH = 9.5

Figure 7 shows the pH decrease in AS from 9.5 (in the 3 days) followed by a steady state at long immersion times. The pH variation in AS was significantly different (P<0.05). Ca^{2+}, Na^+, and Li^+ disrupt the silicate network by non-bridging oxygen including $Si-O- Li^+/Na^+/Ca^{2+}$ bonds. Since the association energy of the Li/O bond (340.5 kcal mol) is higher than Na/O (270 kcal mol), Na^+ ions form more non-bridging oxygen. Thus, durability in basic pH increased by lithium substitution.

In fact, the tendency of basic oxide formation is higher with the decreasing of element electronegativity [23].

Thus, since Li^+ has higher electronegativity than Na^+ ion, it will decrease the basicity of the glasses. As a consequence, the reactivity of lithium bearing glass with the acid phases will be reduced.

Figure 8 shows the weight loss of samples in the first week. There was a noticeable difference in degradation for AS (P<0.05). In basic media, chemical durability is enhanced by Li in the specimens.

The protection of glasses against degradation in contact with water is a significant clinical success. Consequently, chemical composition, pH storage media, and immersion time have a noticeable effect on degradation of glass.

Figure 9 shows the particle morphology after the soaking in AS solution. After immersion of samples in media solution for 14 days, the surface of particles becomes smoother and their morphologies change to globular, which is associated to glass degradation.
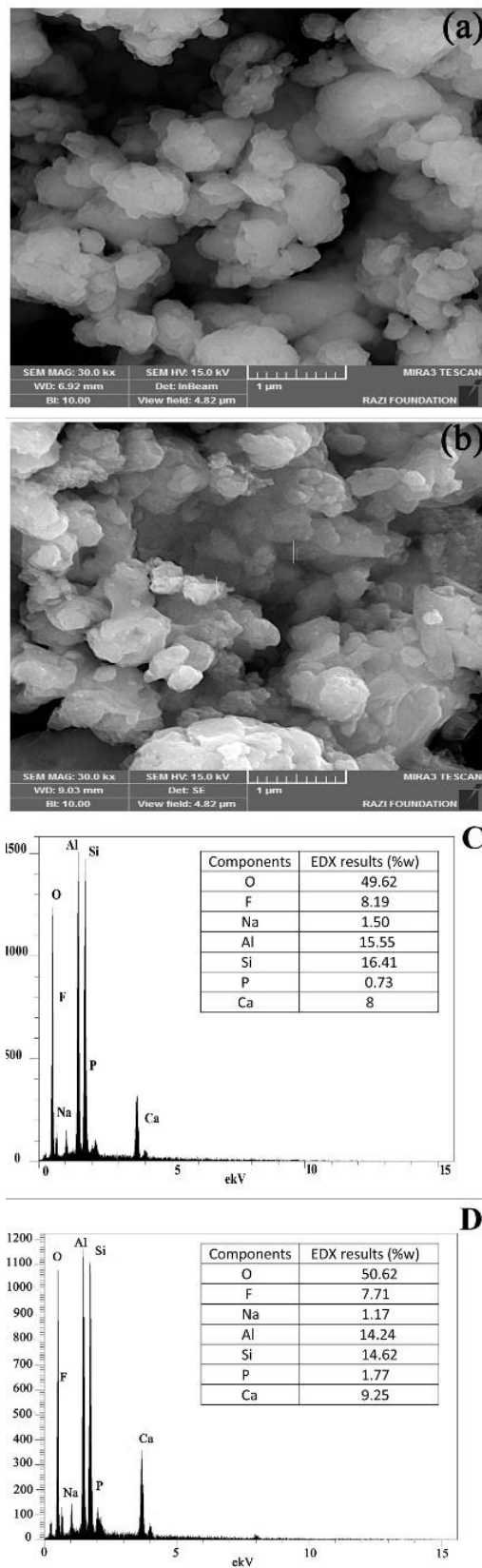
According to the EDS results (Figure 9), the chemical analysis of G4 has not changed (before and after immersion). The reduced degradation rate of glasses was related to the Li water-soluble salts with lower solubility than the sodium water-soluble salts [13, 28]

The frequencies at~ 446 cm^{-1} (attributed to the bending vibration of Si-O-Si , Al-O-Al, and Si-O-Si arised from dissolution of the G4 after soaking in AS for 14 days [2]. The results in Figure 10 point to the break of Si-O-Si and Al-O-Si bonds, bringing about release of network and modifier ions and the solubility of glass [25]. Also, the intensity of the band at ~ 3436.17 decreased after immersion. It is justified that the little exchange between modifier ions and hydrogen ions in media at pH>9 occurs. However, at pH <9, wide ion exchanges should be produced [26].

Figure 11 shows the cytotoxicity of GIC. The results of MTT assay show the cytotoxicity of all GICs against G-292 osteoblasts, in which the effect of GICs on viability of cells was improved by Li substitution. The morphologies of cells cultured for 24 h. in the conditioned medium demonstrated better cell spearing on the modified cement. There is no significant difference between cytotoxicity rates of cements (P>0.05).

Components	EDX results (%w)
O	49.62
F	8.19
Na	1.50
Al	15.55
Si	16.41
P	0.73
Ca	8

Components	EDX results (%w)
O	50.62
F	7.71
Na	1.17
Al	14.24
Si	14.62
P	1.77
Ca	9.25

Figure 9. FESEM images and EDS analysis of G4 before (a) and after (b) immersion in artificial saliva for 14 days
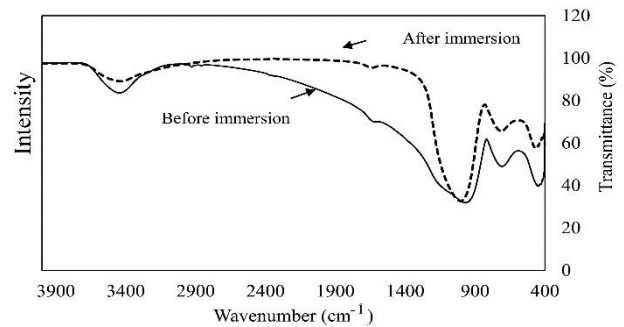
Figure 10. IR spectra of the experimental glass (G4) before and after immersion in AS solution for 14 days
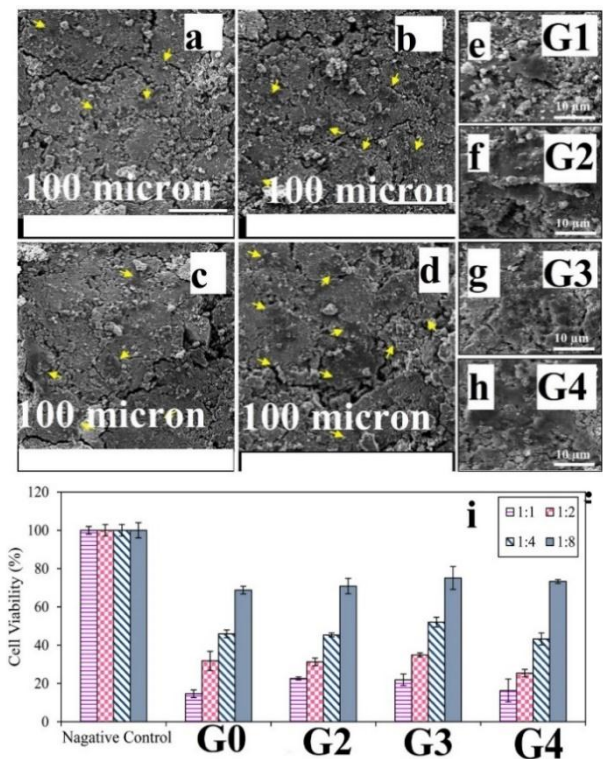
Figure 11. MTT activity of the human osteoblast cells cultured for 24 h in a conditioned medium soaked with cements (G1, G2, G3, and G4) and negative control (diluted by factors 1:2 to 1:8 and undiluted 1:1). SEM images of the human osteoblast (G-292) cells cultured for 24 h in a conditioned medium soaked with cements (a) G1, (b) G2, (c) G3, and (d) G4 with ×1000 magnification, (e) G1, (f) G2, (g) G3, and (h) G4 with 10000 magnification, and (i) the counted Cell in various samples

There was no significant difference in cytotoxicity between experiments (P>0.05). The addition of Li to the dilution of 1:1 and MTT activity has higher cell vitality than Li-free cement (Figure 11). However, this difference was not significant by further dilution (1:2, 1:4, and 1:8). As mentioned earlier, GICs were formed by the reaction

between glass powder and aqueous solution. Dissolution of free ion metals such as Al^{3+}, Ca^{2+}, and Na^+ from the powder to liquid occurred in the mixing process. These ions are non-toxic and do not damage living cells or tissues. Thus, polyacrylic acid in the liquid phase is responsible for cytotoxicity of CICs [34].

4. CONCLUSION

Our research demonstrated the substitution of Li to Na in SiO_2-Al_2O_3-AlF_3-CaF_2-$AlPO_4$-NaF glasses. This study showed that transition temperature, density, network structure, and antibacterial activity were dependent on concentration of Li. G3 (6 wt.% Li) showed higher density than G2 (3 wt.% Li) and G4 (9.2 wt.% Li). The atomic weight or strength field of this ion would be the dominant factor. Also, in Na bearing glass, the disruption of Si-O-Si bonds was hindered by Li. T_g shifted to higher temperatures. It was proved that the breaking of the silicate glasses network in the presence of Na was easier than Li. A decline in the number of non-bridging oxygen was caused by addition of Li. Low atomic weigh of lithium compared to sodium led to the decreased density of synthesized glasses. G4 sample (9.2 wt% Li) showed the highest antibacterial properties. In an acidic environment, the addition of Li to glasses resulted in enhanced solubility. Since breaking Si-O-Si bonds plays a key role in dissolution of glasses in basic pH, the rate of structure disruption was decreased by Li substitution. Justifiably, insigificant exchanges between modifier ions and hydrogen ions in media at pH >9 occurred. However, at pH<9, wide ion exchanges occurred. The observation of FESEM-EDX revealed that the immersion of glass in media solution could make changes in morphologies of the particles caused by the dissolution process.

ACKNOWLEDGEMENT

REFERENCES

1. Forss, H., Widström, E., "Reasons for Restorative Therapy and Longevity of Restorations in Adults", *Acta Odontologica Scandinavica*, Vol. 62, No. 2, (2004), 82-86. https://doi.org/10.1080/00016350310008733

2. Selwitz, R. H., Ismail, A. I., Pitts, N. B., "Dental Caries", *The Lancet*, Vol. 369, No. 9555, (2007), 51-59. https://doi.org/10.1016/S0140-6736(07)60031-2

3. Hengtrakool, C., Pearson, G. J., Wilson, M., "Interaction Between GIC and S. Sanguis Biofilms: Antibacterial Properties and Changes of Surface Hardness", *Journal of Dentistry*, Vol. 34, No. 8, (2006), 588-597. https://doi.org/10.1016/j.jdent.2005.02.011

4. Kidd, E. A. M., Fejerskov, O., "What Constitutes Dental Caries? Histopathology of Carious Enamel and Dentin Related to the Action of Cariogenic Biofilms", *Journal of Dentistry Research*, Vol. 83, No. 1_suppl, (2004), 35-38. https://doi.org/10.1177/154405910408301s07

5. Van Houte, J., Lopman, J., Kent, R., "The Predominant Cultivable Flora of Sound and Carious Human Root Surfaces", *Journal of Dental Research*, Vol .73, No. 11, (1994), 1727-1734. https://doi.org/10.1177/00220345940730110801

6. Caufield, P. W., Li, Y., Dasanayake, A., "Dental caries: an infectious and transmissible disease", *Compendium of Continuing Education in Dentistry (Jamesburg, NJ: 1995)*, Vol. 26, No. 5 Suppl 1, (2005), 10-16. PMID: 17036539. https://pubmed.ncbi.nlm.nih.gov/17036539/

7. Yip, K., Smales, R., "Oral diagnosis and treatment planning: part 2. Dental caries and assessment of risk", *British Dental Journal*, Vol. 213, No. 2, (2012), 59-66. https://doi.org/10.1038/sj.bdj.2012.615.

8. Zamanian, A., Yasaei, M., Ghaffari, M., Mozafari, M., "Calcium hydroxide-modified zinc polycarboxylate dental cements", *Ceramics International*, Vol. 39, No. 8, (2013), 9525–9532. https://doi.org/10.1016/j.ceramint.2013.05.071

9. Yasaei, M., Zamanian, A., Moztarzadeh, F., Ghaffari, M., Mozafari, M., "Characteristics improvement of calcium hydroxide dental cement by hydroxyapatite nanoparticles. Part 1: formulation and microstructure", *Biotechnology and Applied Biochemistry*, Vol. 60, No. 5, (2013), 502-509. https://doi.org/10.1002/bab.1119PMID: 23586755

10. Farrugia, C., Camilleri, J., "Antimicrobial properties of conventional restorative filling materials and advances in antimicrobial properties of composite resins and glass ionomer cements-A literature review", *Dental Materials*, Vol. 31, No. 4. (2015), e89-e99. https://doi.org/10.1016/j.dental.2014.12.005

11. Zamanian, A., Moztarzadeh, F., Kordestani, S., Hesaraki, S., Tahriri, M. R., "Novel calcium hydroxide/nanohydroxyapatite composites for dental applications: In vitro study", *Advances in Applied Ceramics*, Vol. 109, No. 7, (2010), 440-444. https://doi.org/10.1179/174367610X12804792635107

12. Wilson, A. D., Kent, B. E., "The glass-ionomer cement, a new translucent cement dental filling material", *Journal of Applied Chemistry and Biotechnology,* Vol. 21, No. 11, (1971), 313. https://doi.org/10.1002/jctb.5020211101

13. Moshaverinia, A., Roohpour, N., Chee, W. W., Schricker, S. R., "A review of powder modifications in conventional glass-ionomer dental cements", *Journal of Materials Chemistry*, Vol. 21, No. 5, (2011), 1319-1328. https://doi.org/10.1039/C0JM02309D

14. Agha, A., Parker, S., Patel, M. P., "Development of Experimental Resin Modified Glass Ionomer Cements (RMGICs) with Reduced Water uptake and Dimensional Change", *Dental Materials*, Vol. 32, No. 6, (2016), 713-722. https://doi.org/10.1016/j.dental.2016.03.004.

15. Weidlich, P., Miranda, L. A., Maltz, M., Samuel, S. M., "Fluoride release and uptake from glass ionomer cements and composite resins", *Brazilian Dental Journal*, Vol. 11, No. 2, (2000), 89-96. http://www.forp.usp.br/bdj/bdj11(2)/t03112/t03112.html

16. Vermeersch, G., Leloup, G., Vreven, J., "Fluoride release from glass-ionomer cements, compomers and resin composites", *Journal of Oral Rehabilitation*, Vol. 28, No. 1, (2001), 26-32. https://doi.org/10.1046/j.1365-2842.2001.00635.x.

17. Manhart, J., García-Godoy, F., Hickel, R., "Direct posterior restorations: Clinical results and new developments", *Dental Clinics of North America*, Vol. 46, No. 2, (2002), 303-339. https://doi.org/10.1016/S0011-8532(01)00010-6.

18. Randall, R. C., Wilson, N. H. F., "Glass-ionomer restoratives: A systematic review of a secondary caries treatment effect", *Journal of Dental Research*, Vol. 78, No. 2, (1999), 628-637. https://doi.org/10.1177/00220345990780020101.

19. Hu , J., Du, X., Huang, C., Fu, D., Ouyang, X., Wang, Y., "Antibacterial and physical properties of EGCG-containing glass ionomer cements", *Journal of Dentistry*, Vol. 41, No. 10, (2013), 927-934. https://doi.org/:10.1016/j.jdent.2013.07.014.

20. Xie, D., Weng, Y., Guo, X., Zhao, J., Gregory, R. L., Zheng, C., "Preparation and evaluation of a novel glass-ionomer cement with antibacterial functions", *Dental Materials*, Vol. 27, No .5, (2011), 487-496. https://doi.org/ 10.1016/j.dental.2011.02.006.

21. Somani, R., Jaidka, S., Jawa, D., Mishra, S., "Comparative evaluation of microleakage in conventional glass ionomer cements and triclosan incorporated glass ionomer cements", *Contemporary Clinical Dentistry*, Vol. 5, No. 1, (2014), 85-88. https://doi.org/10.4103/0976-237X.128675.

22. Shaiksha Vali, K., Murugan, B. S., Reddy, S. K., Noroozinejad Farsangi, E., "Eco-friendly Hybrid Concrete Using Pozzolanic Binder and Glass Fibers", *International Journal of Engineering*, Vol. 33, No. 7, (2020), 1183-1191. https://dx.doi.org/10.5829/ije.2020.33.07a.03.

23. Rasti; M., Hesaraki; S., Nezafati, N., "An investigation on injectable composites fabricated by 45S5 bioactive glass and gum tragacanth: Rheological properties and in vitro behavior", *Advanced Ceramic Progress*, Vol. 4, No. 2, (2018), 16-26. https://doi.org/10.30501/acp.2018.91121

24. Mosbahi, S., Oudadesse, H., Wers, E., Trigui, M., Lefeuvre, B., Roiland, C., Elfeki, H., Elfeki, A., Rebai, T., Keskes, H., "Study of bioactive glass ceramic for use as bone biomaterial in vivo: Investigation by nuclear magnetic resonance and histology", *Ceramics International*, Vol. 42, No. 4, (2016), 4827-4836. https://doi.org/10.1016/j.ceramint.2015.11.168

25. Huang, X., Yang, T., Zhao, S., Huang, C., Du, X., "Anti-biofilm effect of glass ionomer cements incorporated with chlorhexidine and bioactive glass"**, *Journal of Wuhan University of Technology-Materials Science Edition*, Vol. 27, No. 2, (2012), 270–275. https://doi.org/10.1007/s11595-012-0451-1

26. Elsaka, S. E., Hamouda, I. M., Swain, M. V., "Titanium dioxide nanoparticles addition to a conventional glass-ionomer restorative: influence on physical and antibacterial properties", *Journal of Dentistry*, Vol. 39, No. 9, (2011), 589-598. https://doi.org/10.1016/j.jdent.2011.05.006

27. Lieb, J., "Lithium and antidepressants: stimulating immune function and preventing and reversing infection", *Medical Hypotheses*, Vol. 69, No. 1, (2007), 10-11. https://doi.org/10.1016/j.mehy.2006.12.005

28. Kavitha, R. J., Subha, B., Shanmugam, S., Ravichandran, K., "Synthesis and Invitro Characterisation of Lithium Doped Bioactive Glass through Quick Alkali Sol-Gel Method", (*IJIRSE) International Journal of Innovative Research in Science & Engineering*, Vol. 2, (2014), 2347-3207. https://www.researchgate.net/publication/265249136_Synthesis_and_Invitro_Characterisation_of_Lithium_Doped_Bioactive_Glass_through_Quick_Alkali_Sol-Gel_Method

29. Wang, J., de Boer, J., de Groot, K., "Proliferation and differentiation of osteoblast-like MC3T3-E1 cells on biomimetically and electrolytically deposited calcium phosphate coatings", *Journal of Biomedical Materials Research Part A: An Official Journal of The Society for Biomaterials, The Japanese Society for Biomaterials, and The Australian Society for Biomaterials and the Korean Society for Biomaterials*, Vol. 90, No. 3, (2009), 664-670. https://doi.org/10.1002/jbm.a.32128

30. Hesaraki, S., Gholami, M., Vazehrad, S., Shahrabi, S., "The effect of Sr concentration on bioactivity and biocompatibility of sol–gel derived glasses based on $CaO–SrO–SiO_2–P_2O_5$ quaternary system", *Materials Science and Engineering: C*, Vol. 30, No. 3, (2010), 383-390. https://doi.org/10.1016/j.msec.2009.12.001

31. Akashi, A., Matsuya, Y., Unemori, M ., Akamine, A., "The relationship between water absorption characteristics and the mechanical strength of resin-modified glass-ionomer cements in long-term water storage", *Biomaterials*, Vol. 20, No. 17 , (1999), 1573-1578. https://doi.org/10.1016/S0142-9612(99)00057-5

32. Hanting, C., Hanxing, L., Guoqing, Z., "The setting chemistry of glass ionomer cemen", *Journal of Wuhan University of Technology- Materials Science Edition*, Vol. 20, No. 4, (2005), 110–112. https://doi.org/10.1007/BF02841298

33. Kaur, M., Singh, S. P., Mudahar, D. S., Mudahar, G. S., "Structural B_2O_3-Li_2CO_3-Al_2O_3 Glasses By Molar Volume Measurements and FTIR Spectroscopy", *Materials Physics and Mechanics*, Vol. 15, (2012), 66-73. http://mp.ipme.ru/e-journals/MPM/no_11512/MPM115_06_kaur.pdf

34. Sayyedan, F. S., Fathi, M., Edris, H., Doostmohammadi, A., Mortazavi, V., Shirani, F., "Fluoride release and bioactivity evaluation of glass ionomer: Forsterite nanocomposite", *Dental Research Journal*, Vol. 10, No. 4, (2013), 452-459. https://www.ncbi.nlm.nih.gov/pmc/articles/PMC3793407/

Advanced Ceramics Progress

Research Article

Effect of Microstructure, Chemical Composition, and Open Porosity on Oxidation Resistance of ZrB$_2$-Based Composites

A. Hanifi [a], Z. Balak [a] *

[a] Department of Materials Science and Engineering, Ahvaz Branch, Islamic Azad University, Ahvaz, Khuzestan, Iran

A B S T R A C T

In this research, the effect of microstructure, chemical composition, and open porosity on the oxidation resistance of ZrB2-based composites was investigated. To this end, four composites with different chemical compositions were consolidated by Spark Plasma Sintering (SPS) method in different conditions, namely different temperature, time, and pressure. The open porosity was measured using the Arashmidouse method. Image Analysis Tools (IAT) were also utilized to determine the grain size of all composites through SEM images. For oxidation test, the samples were put on the box furnace and oxidized at 1400 C at different holding times of 20, 40, 60, and 120 minutes. The oxidation resistance was evaluated by weighing the samples before and after oxidation and the Δw was considered as the oxidation criterion. In addition, EDS analysis was used to identify the phases. The results showed that chemical composition was the most significant factor in terms of the oxidation resistance, least affected by open porosity. Sample 9, with a grain size of 2.5 µm and open porosity of 1.5%, had the least oxidation value of 0.0026 gr; however, Sample 4 with a grain size of 12 µm and open porosity of 0.68% had the highest oxidation value of 0.0176 gr.

1. INTRODUCTION

Zirconium diboride or ZrB$_2$ is one of the most investigated materials in the class of Ultra-High Temperature Ceramics (UHTCs) due to its interesting combination of physico-chemical and engineering properties, placing it among the most applicable compounds in the hottest parts of the next-generation aerospace vehicles [1,2].

Since the oxidation resistance is improved by making a composite with additives, ZrB$_2$ does not fully possess the oxidation resistance [3-6] required for surviving the re-entry conditions.

Numerous researchers have investigated the improvement of oxidation resistance of ZrB$_2$-based ceramics [3-6]. Obviously, introduction of compounds containing Si- such as SiC, MoSi$_2$, and WSi$_2$ would enhance the oxidation resistance due to the formation of borosilicate layers on the outer surface of the ZrB$_2$ matrix which acts as the inhibitor of oxygen diffusion.

SiC, regarded among additives as the most effective one, was investigated in compositions with 5–50 vol.% of SiC for ZrB$_2$ in a wide range of test temperatures and pressures in which 20 vol.% compositions were regarded as optimal for hypersonic vehicles in a series of efforts supported by the US Air Force [4-6].

For a composition consisting of 80 vol% ZrB$_2$ and 20 vol% SiC at 1823 K, oxygen diffusivity in the borosilica was evaluated at 1.7×10^{-14} m2/s for a B$_2$O$_3$–21 mol% SiO$_2$ composition which was 10^7 times higher than that for pure silica, yet much lower than that for oxygen in ZrO$_2$ ($\sim 10^{-10}$ m2/s at 1773 K). The refractory ZrB$_2$–SiC system has an eutectic melting temperature of approximately 2573 K [6-10].

* Corresponding Author Email: zbalak1983@gmail.com (Z. Balak)

However, in a condition characterizd by a relatively high temperature and low-oxygen partial pressure, SiC is oxidized in an active mode and its oxidation behaviors at ZrB_2–SiC system are different from those in atmospheric air. Typically, Gao et al. [11] reported that in case the ZrB_2–SiC ceramic was oxidized in low-pressure O_2/N_2 mixture gas, $ZrSiO_4$ began to form at a temperature below 1600 °C. Moreover, they [12] reported that during the oxidation of ZrB_2–SiC composite in low-pressure O_2/N_2 mixture gas at 1500 °C, when the oxygen partial pressure decreased, the oxidation kinetics changed from the parabolic law to the linear law. Moreover, Jin et al. [13] reported the same change for ZrB_2–SiC-Graphite composite when it was oxidized at 1800 °C in low-pressure O_2/Ar mixture gases.

Zapata-Solvas studied the effect of intoducing La2O3 on the oxidation resistance of ZrB_2-20 vol% SiC in the temperature range of 1400−1600 °C [14]. Of note, in this temperature range, the ZrB_2-20 vol% SiC composites exhibited kinetics of mass gain following a power law ($\Delta w_n = kt$) where $1 \leq n \leq 2$, implying that oxidation rates were to be intermediate between those expected from linear and parabolic kinetics; however, introduction of La_2O_3 to the composite would lead to the kinetics based on the parabolic rate law, thus improving the oxidation resistance.

Other researchers have investigated the oxidation behaviors of a ZrB_2–SiC–La_2O_3/SiC dual-layer coating on the siliconized graphite at 1800 °C under low air pressures. In oxidation kinetics, a transition of the coated samples from parabolic weight gain to linear weight loss with a decrease in the air pressure was observed. A protective oxide scale comprising ZrO_2 and SiO_2 with La dispersed was formed on the coating surface after oxidation in 50 kPa air [15].

The kinetics and oxide scale evolution during isothermal exposure of ZrB_2-20 SiC–LaB_6 composites sintered by spark-plasma at 1300 °C in different time periods were examined. The variation of mass gain with time was expressed by near-parabolic rate law during a time period of 0−8 h and by the relations that were suggestive of slower kinetics within 8−24 h, with parabolic rate constants (kp) decreasing sharply [16].

Introducing LaB_6 to ZrB_2-SiC composites would contribute to the oxidation resistance by forming a refractory $La_2Zr_2O_7$ and/or $La_2Si_2O_7$ scale on the outermost surface of oxide scale [17-19].

In our previous study [20], the effect of both different additives, namely SiC, C_f, $MoSi_2$, ZrC, and HfB_2, and SPS conditions, including temperature, time, and pressure, were studied using Taguchi design; in addition, the effect of each variable and its incorporation on the oxidation resistance was determined. In the present study, different compositions and SPS conditions were selected to investigate the effect of microstructure, chemical composition, and open porosity on the oxidation resistance of ZrB_2-based composites.

2. MATERIALS AND METHODS

ZrB_2, SiC, ZrC, C_f, $MoSi_2$, and HfB_2 powders were used as the raw materials. Four composites with different compositions were consolidated by SPS method under different sintering conditions according to Table 1.

First, the weighed powders were ball-milled using zirconia balls through ethanol as milling media in a zirconia cup. The details were expressed elsewhere [12-14]. The process of sintering through spark plasma method was then carried out via SPS furnace (SPS-20T-10: china) in different conditions based on Table 1. To remove the remaining graphite foil, the obtained disk-shaped samples were grinded and then, wire cut to achieve 2×4×10 mm beam-shaped samples for oxidation test. The oxidation test was performed in a box furnace at 1400°C for 20, 40, 60, and 120 min. The weight change was then measured as the oxidation progress criterion, according to the following equation [4-6]:

$$\Delta W_{C-O} \% = \frac{W_i - W_a}{W_i} \times 100 \tag{1}$$

where W_{C-O} shows the percentage of weight change due to oxidation, and W_i and W_a presnet the initial and after-oxidation weights of the samples, respectively.

TABLE 1. Compositions and SPS conditions of four composites

Sample	Factor.1 SiC Vol%	Factor.2 C_f Vol%	Factor.3 (M.t)	Factor.4 $MoSi_2$ Vol%	Factor.5 HfB_2 Vol%	Factor.6 ZrC Vol%	Factor.7 Tem. C	Factor.8 Press. MPa	Factor.9 Time min
4	5	7.5	7.5	6	15	15	1900	40	16
7	10	5	5	6	15	0	1600	20	8
9	15	0	2.5	4	15	0	1700	30	16
13	20	0	2.5	6	10	10	1900	20	4

3. RESULTS AND DISCUSSION

3.1. MICROSTRUCTURAL INVESTIGATION

In order to survey the composite microstructure, SEM images of these four composites were employed, as presented in Fig. 1. According to the previous research [21-23], the black grains are SiC and the dark gray grains are pure ZrB_2. The light phases shown in Composite 7 are HfB_2 and finally, the approximately light phases are (Zr, Hf)B_2 solid solution or ZrC. These approximately light phases can be observed more frequenutly in Composite 7 rather than Composite 4. Moreover, pure HfB_2 (light phase) is not observed in Composite 4. Such differences are observed mainly due to the Hf diffusion to Zr lattice. Based on SPS parameters such as higher temperature, time, and pressure, it can be concluded that diffusion conditions are more supported in Composite 4 than in

Composite 7. In other words, because of the mentioned parameters, the required situation for Hf diffusion and full solution are supported; thus, no pure HfB_2 can be observed.

A comparison of the SEM images shown in Fig. 1 showed that Composite 7 had higher porosity than others. For more investigation, the percentage of open porosity of composites and their grain sizes are given in Table 2. While Composites 4 and 13 had the least open porosity due to the high sintering temperature of 1900 ° C, Composite 7 had the highest open porosity due to the low sintering temperature of 1600 °C.

Compared to Composites 7, 9, and 13, Composite 4 had the largest grain size mainly due to the high temperature and time of SPS and low amount of SiC fucntioning as the grain growth inhibitor. Fine grain microstructure in Composites 7 and 9 was obtained as a result of lower sintering temperatures of 1600 and 1700 °C and higher SiC additive. Although Composite 13 was consolidated at a high sintering temperature of 1900 °C, it had a fine grain size owing to the higher amount of SiC.

To investigate the oxidation resistance and determine the phase formation in composites, the SEM images of cross-sections and their map analysis were employed, as shown in Fig. 2.

Fig. 2 shows the SEM images of the cross-section of Composite 4 after oxidation at 1400 °C at different times. While for Samples 4-20, 4-40, and 4-60, the microstructure of the cross-section contains a black layer with elongated white grains (needle grains), in Sample 4-120, this layer was not found. To identify the phases, both point and map were analyzed, as shown in Figs. 3 and 4. According to the analysis of the points A and B in Fig. 3, this black layer is SiO_2 and the white grains are HfO_2 and ZrO_2. A comparison of the SEM images in Fig. 2 revealed that the microstructure coarsened with oxidation time. Furthermore, it was observed that the number of white grains in the black layer of SiO_2 decreased and the thickness of the oxide layer increased. Reduction of white grains of ZrO_2 and HfO_2 would be indicative of the oxidation resistance with time. Furthermore, an analysis of the map images in Fig. 4 showed the depleted C/Si layer with high thickness, suggesting that in the process of exposing the sample at oxidation atmosphere at 1400 temperature, the oxidation was noticeable.
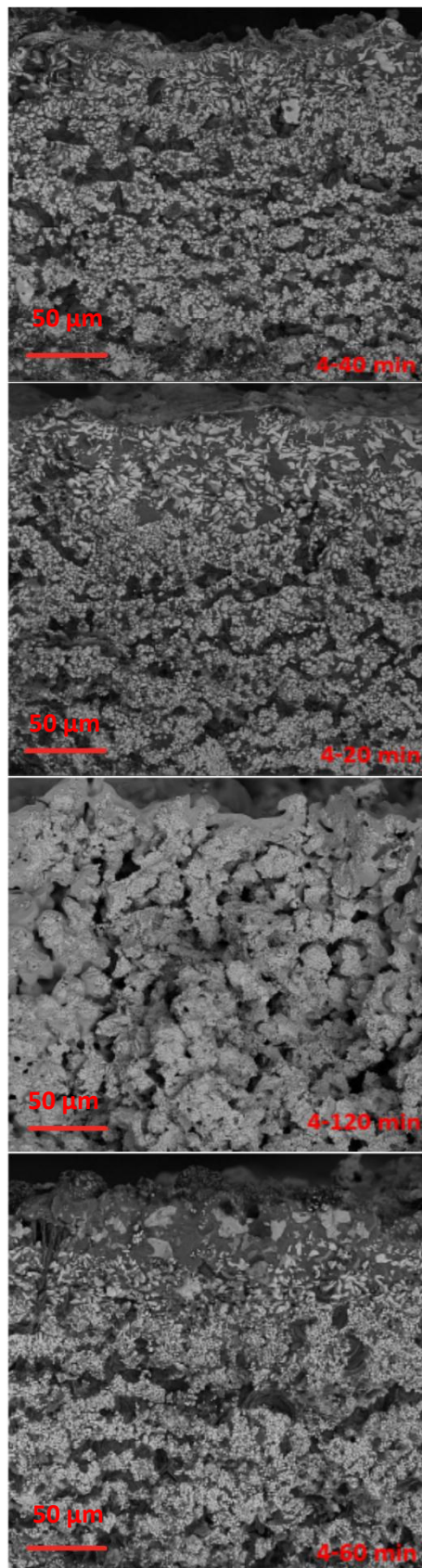
TABLE 2. Open porosity and grain size of all samples

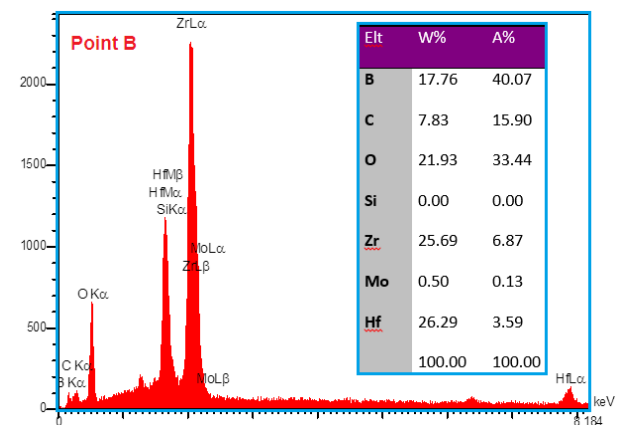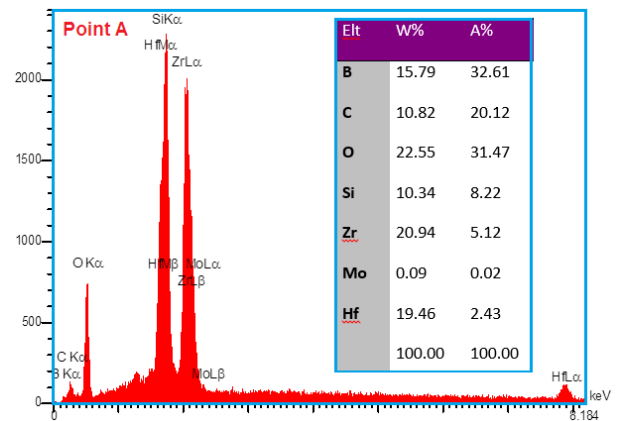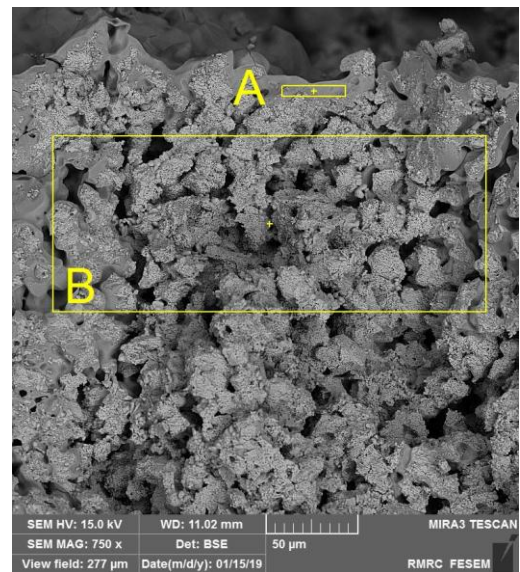| Sample	Average Open porosity %	Grain Size µm
4	0.68	12
7	12.8	2
9	1.1	2.5
13	1.15	3.5
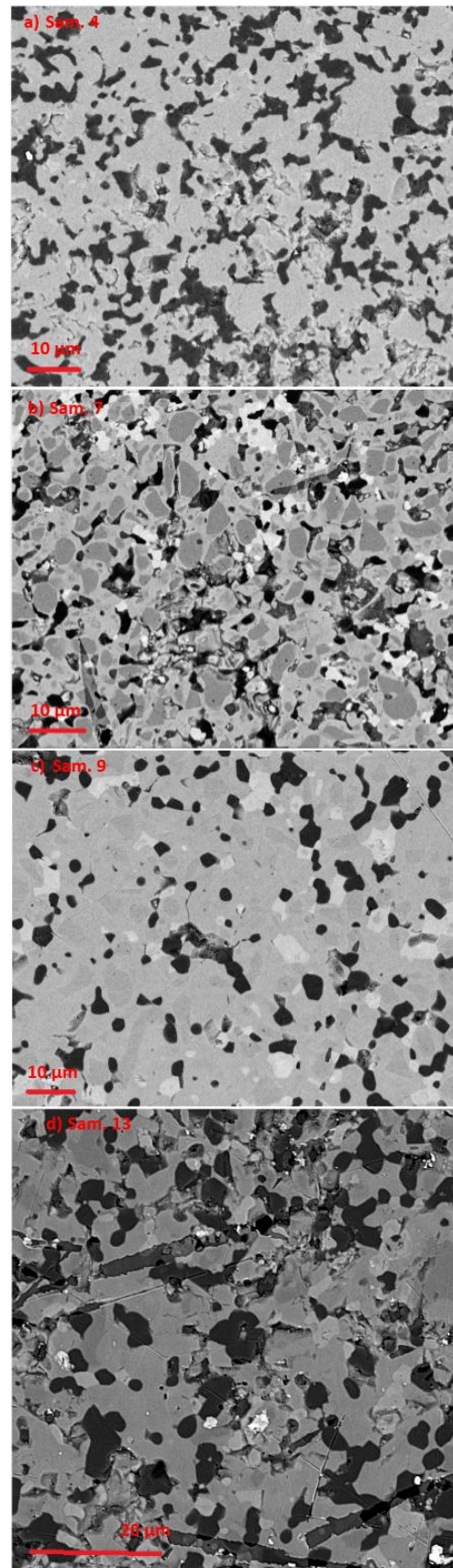
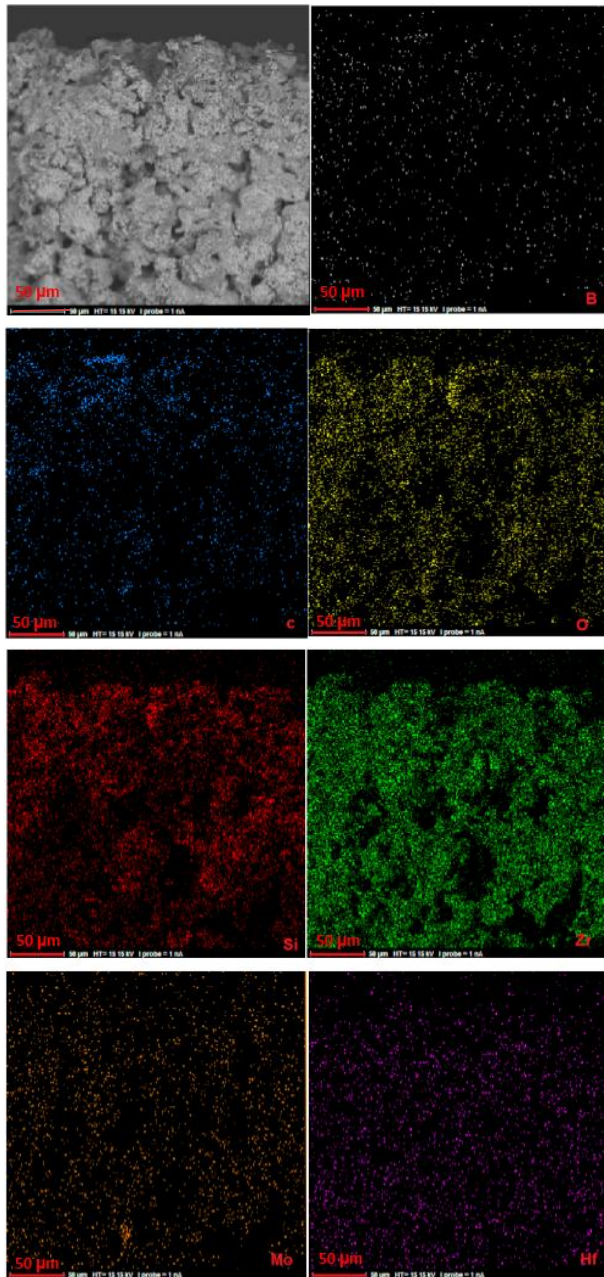**Figure 1.** SEM images of samples a) 4, b) 7, c) 9, and d) 13

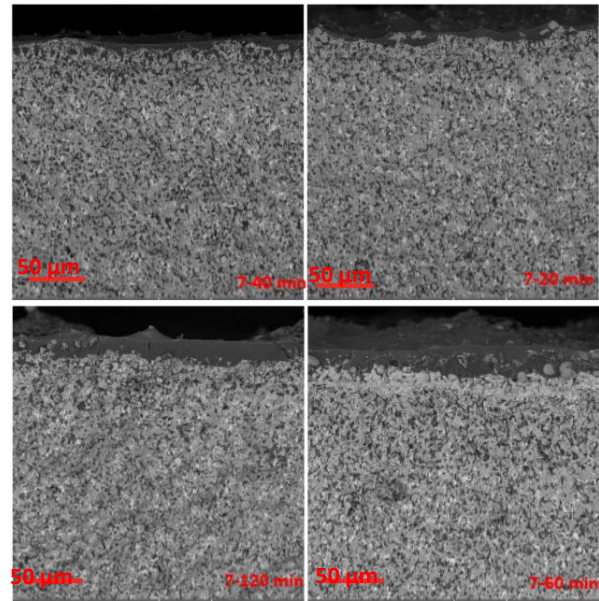**Figure 2.** SEM images of the cross-section of Sample 4 after oxidation at 1400 °C for different times

Figure 3. SEM images and point analysis of Sample 4 after oxidation at 1400 C for 120 min

Fig. 5 presents the SEM images of Sample 7 after oxidation at 1400 °C for different times. Obviously, thickness of the affected zone (oxide zone) increased with oxidation time. Moreover, according to the point

analysis in Fig. 6, the sample surface comprised elements such as O, B, and Si, indicating that this layer was a combination of SiO_2 and B_2O_3 (point A). While at points B and C, the amount of SiO_2 and B_2O_3 decreased noticeably, that of Zr and Hf increased Fig. 7 depicts the SEM images of Samples 9 and 13 at two magnifications after oxidation at 1400 °C for 2 hours. Similar to Samples 4 and 7, the cross-section of Sample 9 contains a SiO_2 black layer with white ZrO_2 grains.

Figure 4. SEM images and map analysis of Sample 4 after oxidation at 1400 C for 120 min

Figure 5. SEM images of cross-section of Sample 7 after oxidation at 1400 C for different times

3.2. OXIDATION RESISTANCE

The SEM images of all samples after oxidation at 1400 °C for 2 hr as well as the thickness of the oxide layer are given in Figs. 9 and 10.

As observed, the microstructure of Sample 4 was different from others that contained more coarse grains and porosities. Coarse garins originated from sintering conditions. Coarse porosites were formed as a result of consumed elements such as Zr, Si, and Hf in ZrC, ZrB_2, SiC, and HfB_2. In fact, the pure ZrB_2 is oxidized at 1100 °C and creates B_2O_3 which evaporates at 1400 °C. SiC reacts with B_2O_3 and produces a SiO_2-B_2O_3 glassy layer. Since SiC amount is low (5 vol%) in this composite, during a two-hour exposure in the oxidation enviroment at 1400 °C, B_2O_3 evaporates and induces porosities in microstructure. Moreover, the very poor oxidation. resistance of ZrC (380 °C), according to the following reaction, promotes porosity formation.

$$ZrC + 2O_2 = ZrO_2(s) + CO_2(g)$$
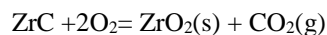
According to Fig. 11, with an increase in the oxidation time, Δw increases which is in total agreement with the thickness of the oxidation layer increment (Figs. 2, 5, 7, and 8).

Δw occurs as a result of greater oxygen diffusion. According to the SEM images of Fig. 9 and oxidation curves in Fig. 11, Sample 9 exhibits different weights vs. oxidation time. Fig. 11 shows a comparison between oxidation values of all samples at different oxidation times.

Among all samples, Samples 7, 13, and 14 exhibited the highest oxidation resistance. Typically, the following factors justify the higher oxidation resistance of Sample 9 than Sample 4: A) larger microstructure grain size in

Sample 9 due to lower sintering temperature (1700 °C) than sample 4 (1900 °C) and higher amount of SiC as grain growth inhibitor (15 Vol% to 5 Vol%5), leading to positive effects on oxidation resistance; (B) chemical composition, according to previous research [21-23], in which SiC reacts with oxygen and creates adhesive SiO_2 layer which noticeably improves the oxidation resistance of ZrB_2-based ceramics.
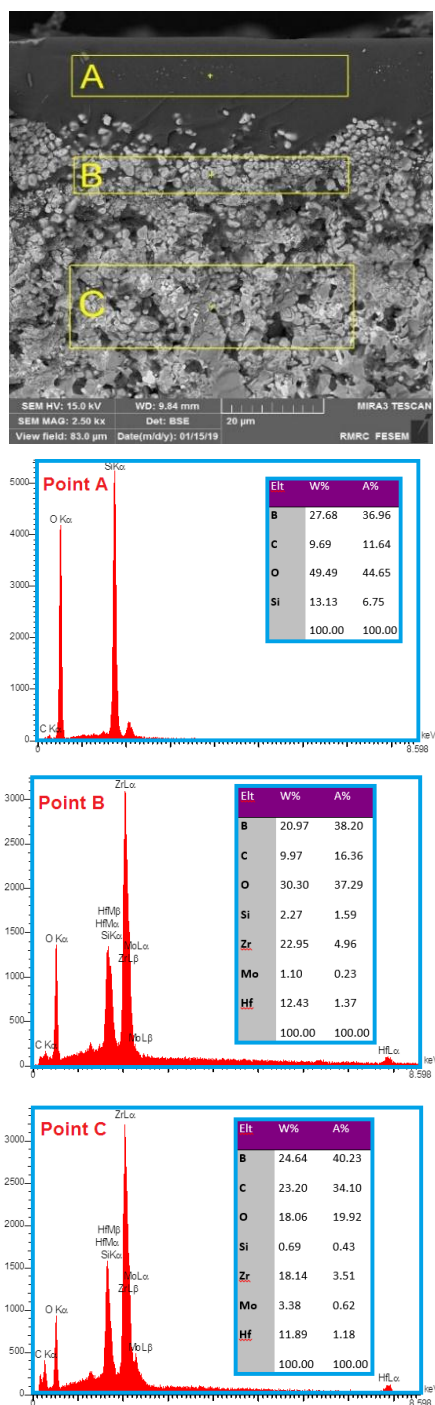

Figure 6. SEM image and point analysis of Sample 7

Sample 9 contains a greater amount of SiC than Sample 4, hence better oxidation resistance. Moreover, the carbon fiber, whose amount is higher in Sample 4, has detrimental effect on the oxidation resistance [21]. Finally, other research has shown that the ZrC is oxided at low temperatures (nearly 600 °C) and its high amount (15 vol%) in Sample 4 resulted in reducing its oxidation resistance rather than Sample 9. Totally, it can be concluded that both the finer microstructure and the desired chemical composition in Sample 9 caused higher oxidation resistance than Sample 4. Open porosity percentage can be an effective factor in oxidation resistance.
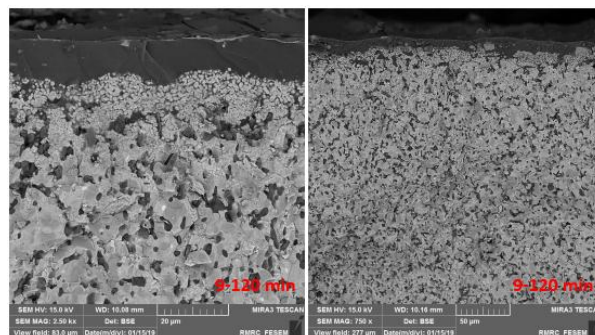
Figure 7. SEM images of the cross-section of Sample 9 after oxidation at 1400 °C for 120 min at two magnifications
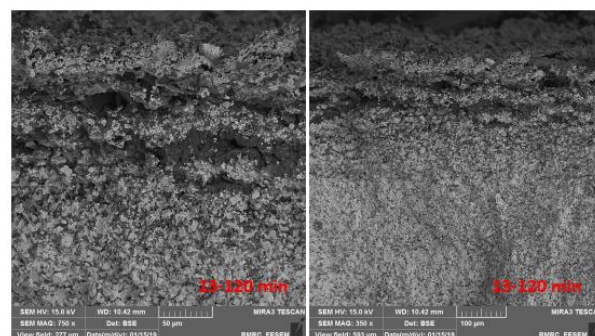

Figure 8. SEM images of the cross-section of Sample 13 after oxidation at 1400 °C for 120 min at two magnifications

Samples 7 and 9 with almost the same chemical compositions and grain sizes were selected for further study. According to Fig. 11, the oxidation resistance of Sample 7 is lower probably due to its higher open porosity, presented in Table 1. Therefore, open porosity by supporting the paths for oxygen diffusion could considerably promote oxygen diffusion to the substrate and reduce the oxidation resistance. Of note, open porosity had the less effect than grain size and chemical composition.

In other words, lower oxidation resistance of Samples 4-13 could be attributed to the coarse grain size, lower SiC, and presence of carbon fiber.

A comparison of Samples 7 and 13 showed that although Sample 7 had higher open porosity, its oxidation resistance was better. With respect to their grain size and

chemical composition, it is clear that both of them have the same grain size with different chemical compositions. Thus, it can be concluded that the chemical composition of Sample 7 is desirable in reaching higher oxidation resistance.
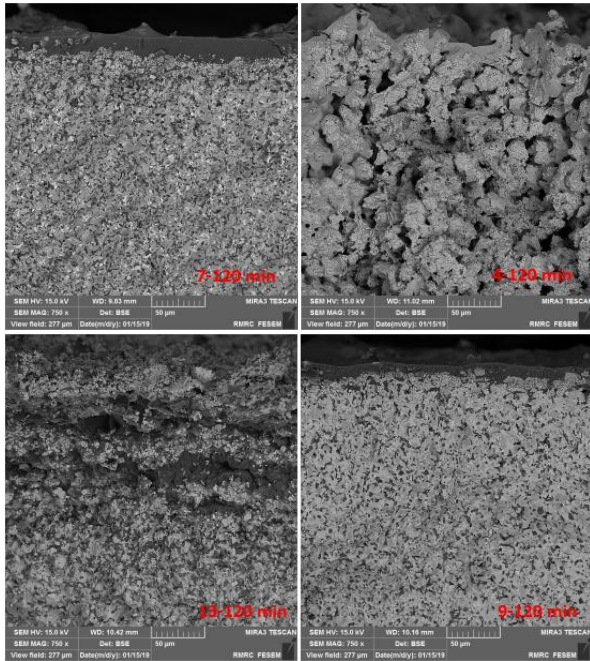
Figure 9. SEM images of the cross-section of all samples after oxidation at 1400°C for 120 min
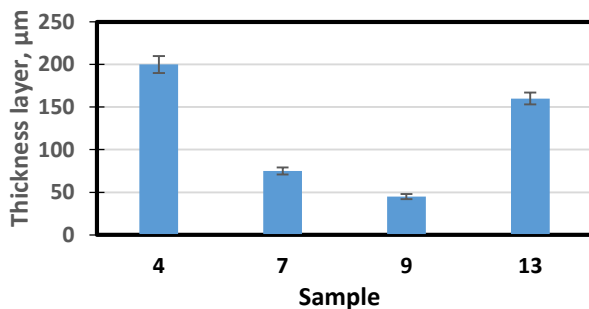
Figure10. Thickness of the oxide layer of all samples after oxidation at 1400 °C for 120 min
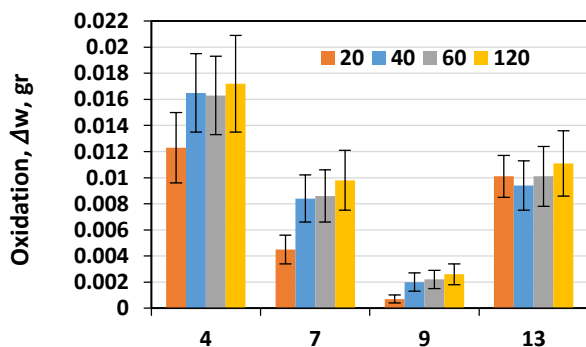
Figure 11. Comparison of weight change of all samples after oxidation at 1400 °C at different times

4. CONCLUSIONS

1- Based on the findings in this study, it can be concluded that factors such as chemical compositions, grain size, and open porosity could considerably affect oxidation resistance, among which chemical composition and open porosity had the most and the least effects, respectively.

2- Among different additives, SiC could significantly improve the oxidation resistance.

3- ZrC and carbon fiber had detrimental effect on the oxidation resistance.

4- During the oxidation at 1400 C, ZrO_2, SiO_2, and HfO_2 phases were formed.

5- The best oxidation resistance (0.0026 gr) was obtained for Composite 9 (ZrB_2-15SiC-15HfB_2-4$MoSi_2$) due to its combination of desirable chemical composition and microstructure (low open porosity and fine grain size).

6- The worst oxidation resistance (0.0176 gr) was obtained for Composite 4 (ZrB2-15ZrC-15HfB_2-7.5C_f -6$MoSi_2$-5SiC) due to its coarse grain size, low SiC amount, and presence of ZrC.

ACKNOWLEDGEMENT

REFERENCES

1. Asl, M.S., Kakroudi, M.G., Nayebi, B., Nasiri, H., "Taguchi analysis on the effect of hot pressing parameters on density and hardness of zirconium diboride", *International Journal of Refractory Metals and Hard Materials*, Vol. 50, (2015), 313-320. https://doi.org/10.1016/j.ijrmhm.2014.09.006

2. George, M. R., "Studies of ultra-high temperature ceramic composite components: synthesis and characterization of HfO_xC_y and Si oxidation in atomic oxygen containing environments", P.H.D Thesis, *Vander Bilt university*, 2008.

3. Guo, W. M., Zhang, G. J., "Oxidation resistance and strength retention of ZrB_2–SiC ceramics", *Journal of the European Ceramic Society,* Vol. 30, No. 11, (2010), 2387–2395. https://doi.org/10.1016/j.jeurceramsoc.2010.01.028

4. Sarin, P., Driemeyer, P.E., . Haggerty, R.P., Kim, D. K., Bell, J.L., Apostolov, Z.D., Kriven, W.M., "In situ studies of oxidation of ZrB_2 and ZrB_2–SiC composites at high temperatures", *Journal of the European Ceramic Society* , V. 30, No. 11, (2010), 2375–2386. https://doi.org/10.1016/j.jeurceramsoc.2010.03.009

5. Rezaie, A. R., . Fahrenholtz, W. G., Hilmas, G. E., "The effect of a graphite addition on oxidation of ZrB_2–SiC in air at 1500 ◦C", *Journal of the European Ceramic Society,* Vol. 33, No. 2, (2013), 413–421. https://doi.org/10.1016/j.jeurceramsoc.2012.09.016

6. Han, J., Hu, P., Zhang, X., Meng, S., Han, W., "Oxidation-resistant ZrB₂–SiC composites at 2200 °C", *Composites Science and Technology*, Vol. 68, No. 3-4, (2008), 799–806. https://doi.org/10.1016/j.compscitech.2007.08.017

7. Rezaie, A., Fahrenholtz, W.G., Hilmas, G.E., "Evolution of structure during the oxidation of zirconium diboride-silicon carbide in air up to 1500 °C", *Journal of the European Ceramic Society*, Vol. 27, No. 6, (2007), 2495–501. https://doi.org/10.1016/j.jeurceramsoc.2006.10.012

8. Fahrenholtz, W.G., "Thermodynamic analysis of ZrB₂–SiC oxidation: formation of a SiC-depleted region", *Journal of the American Ceramic Society,* Vol. 90, No. 1, (2007), 143–148. https://doi.org/10.1111/j.1551-2916.2006.01329.x

9. Williams, P.A., Sakidja, R., Perepezko, J.H., Ritt, P., "Oxidation of ZrB₂–SiC ultra-high temperature composites over a wide range of SiC content", *Journal of the European Ceramic Society*, Vol. 32, No. 14, (2012), 3875–3883. https://doi.org/10.1016/j.jeurceramsoc.2012.05.021

10. Liu, H. L., Liu, J. X., Liu, H.T., Zhang, G.J., "Changed oxidation behavior of ZrB₂–SiC ceramics with the addition of ZrC", *Ceramics International*, Vol. 41, No. 6, (2015), 8247–8251. https://doi.org/10.1016/j.ceramint.2015.02.150

11. Gao, D., Zhang,Y., Fu, J.Y., Xu, C.L., Song, Y., Shi, X.B., "Oxidation of zirconium diboride-silicon carbide ceramics under an oxygen partial pressure of 200 Pa: formation of zircon", *Corrosion science,* Vol. 52, No. 10, (2010), 3297–3303. https://doi.org/10.1016/j.corsci.2010.06.004

12. Tian, C.Y., Gao, D., Zhang,Y., Fu, J.Y., Xu, C.L., Song, Y., Shi, X.B., "Oxidation behaviour of zirconium diboride-silicon carbide ceramic composites under low oxygen partial pressure", *Corrosion science*, Vol. 53, No. 11, (2011) 3742–3746. https://doi.org/10.1016/j.corsci.2011.07.020

13. Jin, H., Meng, S., Xinghong, Z., Qingxuan, Z., Weihua, X., "Oxidation of ZrB2-SiC-graphite composites under low oxygen partial pressures of 500 and 1500 Pa at 1800 °C", *Journal of the American Ceramic Society*, Vol. 99, No. 7, (2016), 2474–2480. https://doi.org/10.1111/jace.14232

14. Zapata-Solvas, E., Jayaseelan, D.D., Brown, P.M., Lee, W.E., "Effect of La2O3 addition on long-term oxidation kinetics of ZrB2-SiC and HfB2-SiC ultra-high temperature ceramics", *Journal of the European Ceramic Society*, Vol. 34, No. 15, (2014), 3535–3548. https://doi.org/10.1016/j.jeurceramsoc.2014.06.004

15. Rena, Y., Qian,Y., Xu, J., Zuo, J., Li, M., "Oxidation resistance and microstructure evolution of ZrB–SiC–La2O3/SiC dual-layer coating on siliconized graphite at 1800 °C under low air pressures", *Ceramics International*, Vol. 46, No. 17, (2020), 27150–27157. https://doi.org/10.1016/j.ceramint.2020.07.195

16. Kashyap, S.K., Kumar, A., Mitra, R., "Kinetics and evolution of oxide scale during various stages of isothermal oxidation at 1300 °C in spark plasma sintered ZrB2 – SiC – LaB6 composites", *Journal of the European Ceramic Society*, Vol. 40, No. 15, (2020), 4997–5011. https://doi.org/10.1016/j.jeurceramsoc.2020.07.053

17. Zhang, X.H., Hu, P., Han, J.C., Xu, L., Meng, S.H., "The addition of lanthanum hexaboride to zirconium diboride for improved oxidation resistance", *Scripta Materialia*, Vol. 57, No. 11, (2007), 1036–1039. https://doi.org/10.1016/j.scriptamat.2007.07.036

18. Jayaseelan, D.D., Zapata-Solvas, E., Brown, P., Lee, W.E., "In situ formation of oxidation resistant refractory coatings on SiC-reinforced ZrB2 ultra high temperature ceramics", *Journal of the American Ceramic Society*, Vol. 95, No. 4, (2012), 1247–1254. https://doi.org/10.1111/j.1551-2916.2011.05032.x

19. Hu, P., Zhang, X.H., Han, J.C., . Luo, X.G, Du, S.Y., "Effect of various additives on the oxidation behavior of ZrB2-based ultra-high-temperature ceramics at 1800°C", *Journal of the American Ceramic Society*, Vol. 93, No. 2, (2010) 345–349. https://doi.org/10.1111/j.1551-2916.2009.03420.x

20. Balak, Z., Azizieh, M., "Oxidation of ZrB₂-SiC composites at 1600 ℃: Effect of carbides, borides, silicides, and chopped carbon fiber", *Advanced Ceramics Progress*, Vol. 4, No, 1, (2018), 18-23. https://dx.doi.org/10.30501/acp.2018.90829

21. Balak, Z., Zakeri, M., Rahimipour, M., Salahi, E., "Taguchi design and hardness optimization of ZrB2-based composites reinforced with chopped carbon fiber and different additives and prepared by SPS", *Journal of Alloys and Compounds*, Vol. 639, (2015), 617–625. https://doi.org/10.1016/j.jallcom.2015.03.131

22. Balak, Z., Zakeri, "Application of Taguchi L₃₂ orthogonal design to optimize flexural strength of ZrB₂-based composites prepared by spark plasma sintering", *International Journal of Refractory Metals and Hard Materials*, Vol. 55, (2016), 58–67. https://doi.org/10.1016/j.ijrmhm.2015.11.009

23. Balak, Z., Zakeri, M., Rahimipoor, M.R., Salahi, E., Azizieh, M., Kafashan, H., "Investigation of Effective Parameters on Densification of ZrB₂-SiC Based Composites Using Taguchi Method", *Advanced Ceramics Progress*, Vol. 2, No. 2, (2016), 7-15. https://dx.doi.org/10.30501/acp.2016.90835

AIMS AND SCOPE

Advanced Ceramics Progress (ACERP) as an ISC international journal is devoted to elucidating the fundamental aspects of chemistry and physics occurring at a wide range of oxide and nonoxide ceramics and composite materials and their processing, microstructure, properties, and applications. The journal provides a unique venue for publishing new exciting research, focusing on dynamic growth areas in this field.

INSTRUCTIONS FOR AUTHORS

Submission of manuscript represents that it has neither been published nor submitted for publication elsewhere and is result of research carried out by author(s).

Authors are required to include a list describing all the symbols and abbreviations in the paper. Use of the international system of measurement units is mandatory.

- On-line submission of manuscripts results in faster publication process and is recommended. Instructions are given in the ACERP web site: www.acerp.ir
- Hardcopy submissions must include MS Word and jpg files.
- Manuscripts should be typewritten on one side of A4 paper, double-spaced, with adequate margins.
- References should be numbered in brackets and appear in sequence through the text. List of references should be given at the end of the paper.
- Figures' captions are to be indicated under the illustrations. They should sufficiently explain the figures.
- Illustrations should appear in their appropriate places in the text.
- Tables and diagrams should be submitted in a form suitable for reproduction.
- Photographs should be of high quality saved as jpg files.
- Tables, illustrations, figures and diagrams will be normally printed in single column width (8 cm). Exceptionally large ones may be printed across two columns (17 cm).

PAGE CHARGES AND REPRINTS

ACERP subscribers do not need to make any payment for publication and reprints.

AUTHORS CHECKLIST

- Author(s), bio-data including affiliation(s) and mail and e-mail addresses.
- Manuscript including abstract, key words, illustrations, tables, figures with figures' captions and list of references.
- MS Word files of the paper.

Advanced Ceramics Progress

Volume 6, Number 4, Autumn 2020

CONTENTS